MODELLISTICA E CALCOLO SCIENTIFICO

MOX

MODELING AND SCIENTIFIC COMPUTING

MOX–Report No. 31/2010

Shape optimization for viscous flows by reduced basis methods and free-form deformation

ANDREA MANZONI, ALFIO QUARTERONI, GIANLUIGI ROZZA

Shape optimization for viscous flows by reduced basis methods and free-form deformation

Andrea Manzoni$^\sharp$, Alfio Quarteroni$^{\sharp,\dagger}$, Gianluigi Rozza$^{\sharp*}$

August 26, 2010

$^\sharp$ CMCS - Modelling and Scientific Computing,
MATHICSE - Mathematics Institute of Computational Science and Engineering,
EPFL - Ecole Polytechnique Fédérale de Lausanne,
Station 8, CH-1015 Lausanne, Switzerland.

† MOX– Modellistica e Calcolo Scientifico,
Dipartimento di Matematica "F. Brioschi",
Politecnico di Milano,
via Bonardi 9, 20133 Milano, Italy.

Keywords: Model order reduction; Reduced basis methods; Free form deformation; Shape optimization; Haemodynamics; Stokes equations

Abstract

In this paper we present a new approach for shape optimization that combines two different types of model reduction: a suitable low-dimensional parametrization of the geometry (yielding a geometrical reduction) combined with reduced basis methods (yielding a reduction of computational complexity). More precisely, free-form deformation techniques are introduced for the geometry description and its parametrization, while reduced basis methods are used upon a finite element discretization to solve systems of parametrized partial differential equations. This allows an efficient flow field computation and cost functional evaluation during the iterative optimization procedure, resulting in effective computational savings with respect to usual shape optimization strategies. This approach is very general and can be applied for a broad variety of problems. To prove its effectivity, in this paper we apply it to find the optimal shape of aorto-coronaric bypass anastomoses based on vorticity minimization in the down-field region. Stokes equations are used to model blood flow in the coronary arteries.

*Corresponding Author, E-mail: `gianluigi.rozza@epfl.ch`

1 Introduction and Motivation

The efficient solution of optimal control or shape optimization problems involving partial differential equations (PDEs) is a problem of interest for cardiovascular surgeons and computational scientists. The goal is the minimization/maximization of a given cost functional under some (algebraic, topological or differential) constraints, controlling either suitable variables (such as sources, model coefficients or boundary values) or the shape of the domain itself. In this paper we focus on the latter class of problems referred as *shape optimization* or *optimal shape design* problems [1, 2, 3, 4]. In fluid mechanics, cost functionals are expressed in terms of flow variables (such as velocity, pressure, temperature, etc.), while constraints are usually given under the form of PDEs (advection-diffusion, Stokes or Navier-Stokes equations, etc.) describing the flow, besides topological constraints on the shape of the domain, if necessary.

In a broad variety of applications the design of devices able to reduce drag forces, dissipations or stresses greatly enhances the efficiency of a system. The reduction of drag in transportation vehicles (aircrafts, watercrafts) and of vorticity and stresses in biomedical devices, and the compliance minimization in cantilevers or membranes represent further instances in which shape optimization techniques are called into play.

For the numerical solution of these problems, efficient procedures are required since (i) PDEs are expensive to solve when solutions need to capture fine details (such as velocity and thermal boundary layers, vorticity structures, etc.); (ii) the finite element assembling discretization procedures result expensive when problem geometry keeps changing; (iii) optimization requires recursive evaluations of the cost functional. For example, a classical shape optimization algorithm based on explicit boundary displacement, even though able to give accurate solutions, proves to be very unefficient, since at each step PDEs problems have to be solved for a new geometrical configuration. A key to simplification consists of making use of a reference configuration on which every problem is brought back and solved at each iteration of the optimization process, and geometry variations are accounted for the equation coefficients.

The introduction of a suitable (low-dimensional) shape parametrization is thus instrumental to reduce both the geometrical and computational complexity. Obviously, shape parametrization has to be flexible enough to describe a wide family of admissible shapes without substantially increasing the number of parameters and, at the same time, it should be computationally efficient to allow for a fast solution of the parametrized PDEs. Free-form deformation techniques [5, 6, 7] provide a powerful tool for representing global and smooth deformations acting on a small number of design parameters. Once the shape has been parametrized, we solve iteratively a partial differential (state) equation and evaluate the cost functional we want to minimize on the parametric domain. To do this, we rely on reduced basis methods for parametrized partial differential equations (P^2DEs) (see the review papers [8, 9]). Thanks to a suitable compu-

tational *Offline-Online* decomposition (see Sec. 6), RB methods provide rapid and reliable results at a greatly reduced cost, and are well-indicated above all in real-time (e.g. parameter estimation) and multi-query (e.g. optimization, control) contexts. The combination of free-form deformation techniques with reduced basis methods allows a considerable geometrical (i.e. with respect to the number of design parameters) as well as computational (in terms of linear system dimensions of the resulting discretized problems) reduction.

Our proposed approach to parametric shape optimization is as follows. First we introduce the mathematical formulation for parametric PDEs problems. Then, a suitable parametrization of the geometry is obtained by using free-form deformation (FFD): this technique allows to build a parametric map through which we reformulate our original problem on a reference configuration, resulting in a parametrized problem where the effect of geometry variations is traced back onto its parametrized transformation tensors. Since FFD techniques lead (in general) to non-affinely parametrized transformations of the computational domain, we approximate their components by means of affinely parametrized tensors, through the empirical interpolation method (EIM) [10, 11, 12, 13]. In this way, we can perform a suitable Offline-Online computational strategy, through which reduced basis approximation gives a rapid and reliable field solution and cost functional evaluation. At the outer level, this is used in a suitable iterative procedure for the (now, parametric) optimization.

The proposed approach is rather general and can be used in a broad variety of application contexts. To provide a proof of its efficacy, in this paper we apply it to the design of cardiovascular prostheses. More specifically, the design of a bypass graft has been formulated as a shape optimization and flow control problem in [14] and later studied using small perturbation techniques and an asymptotic development in Agoshkov et al. [15, 16]. The reduced basis framework applied to the Stokes problem approximation has been used to study a simple bypass design problem in presence of either affine or nonaffine shape parametrization, treating some shape geometrical dimensions (such as lenghts, diameters, angles) as design parameters (see [13, 17, 18]).

In this paper we aim at extending this framework, by handling more general shape parametrizations in order both *(i)* to enrich the family of possible shape configurations and *(ii)* to combine the RB framework with more unspecific tools for an efficient shape treatment, where (possibly) the parametric shape deformations result independent of the problem geometry, the flow model and the computational mesh. The approach we propose is in fact based on the coupling of three different tools – free-form deformation, empirical interpolation and reduced basis methods – and applied to steady incompressible Stokes equations.

This combined "RB+FFD" approach features several advantages: it is very flexible, it involves the solution of low dimensional problems (with low geometrical dimension), yielding substantial computational savings without sacrificing numerical accuracy, even when addressing complex shape optimization problems.

Needless to say, techniques and methods discussed in this work prove to be useful also in facing other optimization problems arising in haemodynamics and, more generally, in computational fluid dynamics.

The paper is organized as follows. In Sec. 2 we address the medical and bioengineering aspects of bypass surgery. In Sec. 3 we present a review of reduction strategies for shape optimization problems and illustrate our proposed approach to parametric shape design, then in Sec. 4 we study the mathematical modelling of the problem. In Sec. 5 we introduce free-form deformation techniques for shape parametrization, while in Sec. 6 we deal with reduced basis methodology and formulate the reduced basis approximation of the optimal bypass design problem. In Sec. 7 we deal with optimization and algorithmic aspects, then in Sec. 8 we introduce numerical results and address a brief comparison with the previous ones. In the last Sec. 9 we sketch some possible future developments and improvements.

2   Bypass surgery: medical & bio-engineering aspects

Aorto-coronaric bypass graft surgery represents the standard treatment of advanced coronary arteries diseases. Coronary circulation is the circulation of blood in vessels of the heart muscle; in particular, coronary arteries deliver oxygen-rich blood to the myocardium. In fact, when a coronary artery is affected by atheromatous plaques or a stenosis, the heart muscle does not receive the necessary oxygen amount through blood circulation: aorto-coronaric anastomosis thus restores the oxygen amount through a bypass surgery downstream an occlusion (see Fig. 1).
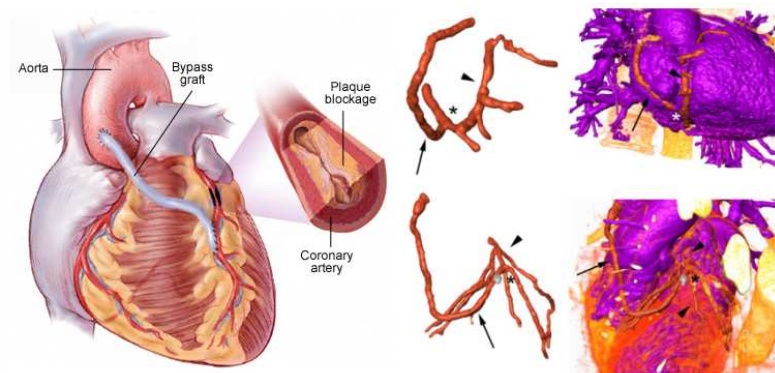

Figure 1: Left side: heart, coronary arteries and bypass graft. Right side: anatomical depiction of end-to-side and side-to-side models including the aorto-coronary bypasses (arrows), the coronary arteries (arrowheads), the anastomosis (asterisks) and their relation to the heart and aorta. Picture taken from *Biomed. Eng. Online, 35(6), 2007*.

Different kind and shape for aorto-coronaric bypass anastomoses are available (e.g. Miller cuffed models, Taylor patches, etc.) and consequently different surgery procedures are used to set up a bypass; in general, the connection of the graft to the coronary artery can be done using an end-to-side or a side-to-side anastomosis. For a discussion and a comparative approach see, for example, Cole et al. [19, 20]. Bypass can be made by organic material (e.g. the saphena vein taken from patients legs or the mammary artery) or by prosthetic material. The graft patency affects the long-term efficacy of coronary bypass procedures, and several post-surgical complications have to be taken into consideration. Among them, we mention intimal thickening hyperplasia (near suture lines), which is a narrowing of coronary arteries, restenosis, surgical injury, long term graft failure. In particular, during the first year after bypass surgery up to 15% of venous graft occlude, while by ten years after only 60% of vein grafts are patent and only 50% of patent vein grafts are free of significant stenosis [21, 22]. Moreover, every year 8% of all patients risk bypass occlusion, after ten years 80% bypasses must be replaced (these statistics refer to the situation in the U.S.A.). One of the most important process is atherosclerotic obstruction occurring on a foundation of neointimal hyperplasia. This thickening, which results from an accumulation of muscle cells and extracellular matrix in the intimal compartment, is the principal disease process in venous bypass grafting during the first post-surgical year and represents the foundation for later development of graft atheroma and atheromatous plaques.

Computational fluid dynamics (CFD) helps understanding local haemodynamics phenomena and the effect of vascular wall modication on flow patterns (e.g. [23]). This can have useful clinical applications especially in surgical procedures. In the case of bypass grafting, correlations between low and oscillatory wall shear stress (WSS) or high vorticity areas and atherogenesis or intimal hyperplasia have been established [24]. Moreover, computational studies have highlighted the correlation between geometric configurations and vorticity, shear stress, shear stress gradient [25] and oscillatory shear index [13], as effect of recirculation, flow separation and moving stagnation zones [19, 20, 21]. For the problem at hand, we are interested in the minimization of the blood vorticity in the down-field region of the bypass by changing the shape of the anastomosis. In fact, high vorticity areas are responsible of atherogenesis or intimal hyperplasia, which can eventually lead to the failure of grafting surgery. The design of artificial arterial bypass is a very complex problem; recent analysis on parametrized bypass graft configurations [25, 26, 27] have shown a deep influence of anastomotic angle and graft-artery diameter ratio on WSS distribution.
In this work we want to improve the results already obtained [14] by developing new tools of model order reduction and formulating the problem as a suitable parametrized shape optimization problem. We aim at demonstrate the potential role of shape optimization techniques in designing bypass grafts, coupled with (i) suitable low-dimensional shape parametrization techniques for the configu-

ration description (and reduction of geometrical complexity) and (ii) reduced basis methods for the solution of parametric PDEs problems and computational reduction.

3 Model Order Reduction strategies in Shape Optimization

The example addressed in the previous section represents an instance where the design of an optimal configuration arises in a *(i) user-dependent* (e.g. patient-specific in the case of a bypass), *(ii) real-time* (since we could be interested in a very rapid solution) and *(iii) many-query* (since optimization requires repetitive evaluations of different configurations) contexts. In this scenario, suitable parametrization techniques and reduced basis methods allow to obtain more efficient methods.

In particular, we consider an output of interest as a function of an input parameter P-vector $\boldsymbol{\mu}$ related to geometry, physical properties, boundary conditions or sources; the input parameter domain is denoted as $\mathcal{D} \subset \mathbb{R}^P$. The output of interest $s(\boldsymbol{\mu})$ is (in our case, say a quadratic) functional of a field variable $u(\boldsymbol{\mu})$, $s(\boldsymbol{\mu}) = J(u(\boldsymbol{\mu}))$, where $u(\boldsymbol{\mu})$ satisfies a PDE parametrized with respect to $\boldsymbol{\mu}$. We thus arrive at an input–output statement $\boldsymbol{\mu} \rightarrow s(\boldsymbol{\mu})$ evaluation of which requires to solve a parametrized partial differential equation (P^2DE). The possibility of performing this evaluation in a very rapid way is crucial in optimal control problems, where we might need to execute iteratively a large amount (say, $\mathcal{O}(10^2)$) of these operations. For this kind of problems, input parameters can be divided into three classes: control (i.e depending, in some way, on control function), physical (like velocity field or diffusivity) and geometrical (i.e. related to different domain conguration). On the other hand, the output of interest $s(\boldsymbol{\mu})$ is the cost functional which has to be minimized, while the underlying P^2DE gives the (state) constraint. By suitable parametrizations, shape optimization problems can be recast as optimal control problems dealing with geometrical (or design) parameters as control variables. The problem we consider in this work is related both to optimal design and flow control [28, 29, 4]. Indeed, we refer to *parametric shape optimization* [1] when dealing with a flow control through the optimization of the parametrized shape of the domain crossed by the flow itself.

A crucial point in shape optimization is the definition of the set of admissible shapes under which optimization can be performed. Following an increasing level of reduction, three different approaches can be envisaged:

- *Topological Shape Optimization*: in the most general case, we deal with the optimization of a shape by acting, during the optimization process, both on the position of its free boundary and on its topology [1, 30], as for example the inclusion of holes.

- *Geometrical Shape Optimization*: very often, the problem is formulated as the minimization of a cost functional (depending on both the shape and the solution of a PDE system) on a set of shapes with fixed topological properties; the position of the domain boundary under control is changed during the optimization process [31, 32, 33].

- *Parametric Shape Optimization*: this third approach is based on the possibility to describe the shape by means of some input parameters [1] and it is naturally the best framework where reduced basis methods for P^2DEs can be introduced. Depending on the role played by input parameters, we can obtain three different subcases, depicted in Fig. 2:

  1. input parameters are *geometrical properties* (e.g. lenghts, angles, diameters, etc.) that identify different configurations in a family of shapes chosen *a priori*. In this way we obtain a simple but often restrictive description of domain shapes. For example, bypass configurations have been modeled as "T-shaped" domains with a curved incoming branch in previous works [13, 9, 18];

  2. input parameters are *variables describing shape boundary*, by means of explicit boundary parametrization or else involving given shapes families (such as Bézier curves, B-splines [34, 35], etc.). The family of admissible shapes is thus wider, however shape deformations still depend on reference configuration and computational mesh;

  3. input parameters are *free-form parameters*, such as perturbations applied to a lattice of mesh-independent control points [5, 36, 6, 7]. In this case design parameters are not directly connected to geometrical properties, neither to the shape boundary we want to optimize.

With respect to the geometrical shape optimization, the parametric shape optimization framework allows to reach increasing levels of complexity reduction (see the review [37] for a comparison of different options). In particular, free form deformation techniques realize a very good trade-off between shape flexibility and using a low number of parameters, allowing therefore to achieve global computational efficiency by using a low dimensional optimization space [3]. A detailed description of this method will be provided in Sec. 5.

4 Mathematical modelling and parametrized PDEs

In the perspective of using low order methods for shape optimization, we adopt the steady Stokes (rather than the more appropriate Navier-Stokes) equations for modelling low Reynolds blood flow in mid size arteries [23, 14], like e.g. the coronary arteries. Besides, because of flow pulsatility we should consider unsteady
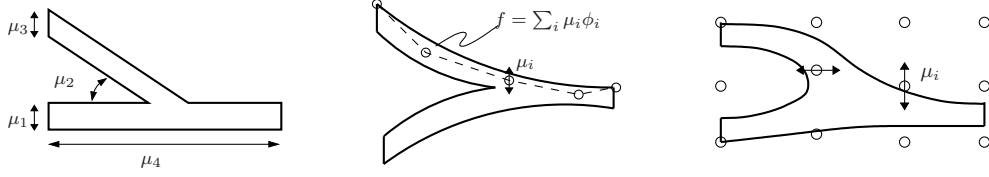
Figure 2: Different parametrization approaches: input parameters as geometrical properties (left), as variables describing shape boundary through a shapes family $\{\phi_i\}_{i \in I}$ (middle), as free-form parameters (right).

equations, however such a model would be too complex in view of reducion strategies for shape optimization, since we would deal with time-dependent domain shapes (because of the heart beat). Once we get results from the shape optimization procedure using this low fidelity approach, we have to test it with a higher fidelity model, as proposed in [14]. With the goal of reducing blood vorticity in the down-field zone of the incoming branch of the bypass, we introduce a suitable parametric output (expressed as a functional of field variables) to be minimized.

4.1 Geometry description, state equations, system observation

To model the incoming branch of a bypass we consider a longitudinal section in the mean plane and the corresponding two-dimensional domain $\Omega_o := \Omega_o(\boldsymbol{\mu})$, whose shape is depending on a set of $P \geq 1$ geometrical parameters $\boldsymbol{\mu} = (\mu_1, \ldots, \mu_P) \in \mathcal{D} \subset \mathbb{R}^P$. The original domain $\Omega_o(\boldsymbol{\mu})$ can be seen as obtained by a reference domain Ω through a regular parametric domain map $T(\cdot; \boldsymbol{\mu}) : \Omega \to \mathbb{R}^2$. The steady Stokes equations [38] in $\Omega_o(\boldsymbol{\mu})$ read as follows:

$$
\begin{cases}
-\nu \Delta \mathbf{v}_o + \nabla p_o = \mathbf{f}_o & \text{in } \Omega_o(\boldsymbol{\mu}) \\
\nabla \cdot \mathbf{v}_o = 0 & \text{in } \Omega_o(\boldsymbol{\mu}) \\
\mathbf{v}_o = \mathbf{0} & \text{on } \Gamma_w^o \\
\mathbf{v}_o = \mathbf{g}^D & \text{on } \Gamma_{in}^o \\
-p_o \mathbf{n} + \nu \dfrac{\partial \mathbf{v}_o}{\partial \mathbf{n}} = \mathbf{g}^N & \text{on } \Gamma_{out}^o,
\end{cases}
\tag{1}
$$

where $(\mathbf{v}_o, p_o)$ are the velocity and the pressure fields, for some given $\mathbf{f}_o$, $\mathbf{g}^D$, $\mathbf{g}^N$; $\mathbf{n}_o$ is the normal unit vector on the boundary $\partial \Omega_o(\boldsymbol{\mu})$, which is partitioned in three components (see Fig. 3): Γ_{in}^o is the inflow boundary, Γ_{out}^o the outflow boundary and Γ_w^o the boundary corresponding to the arterial wall.

We set $\Gamma_D^o = \Gamma_{in}^o \cup \Gamma_w^o$. The inflow boundary Γ_{in}^o is given by two different inflow sections: the bypass inflow section Γ_b^o and the stenosed artery section Γ_a^o. No-slip conditions are imposed on Γ_w, while homogeneous (free-stress) Neumann conditions are imposed on the outflow section Γ_{out}^o. Concerning inflow boundary conditions, we impose a Poiseuille parabolic profile on Γ_b^o. Indeed, the Womersley number [23] for blood flow in coronary arteries is $Wo \approx 2.1$ and a
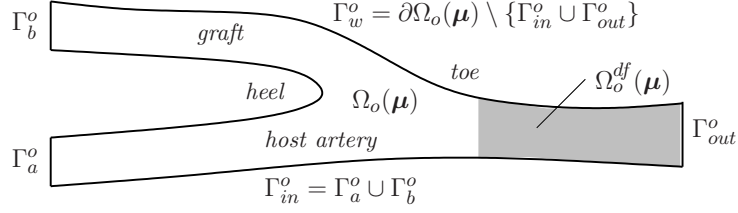
Figure 3: Idealized two-dimensional bypass anastomosis and notation used for domain and boundary; $\Omega_o^{df}(\boldsymbol{\mu})$ is the down-field region where observation will be made.

steady Womersley profile can be assimilated at a simpler Poiseuille flow. Then we consider two different cases for the artery section Γ_a^o, according that we have either complete occlusion ($\mathbf{g}^D = 0$ on Γ_a^o) or a partial occlusion (residual flow $\mathbf{g}^D \neq 0$ on Γ_a^o). Inflow peak velocity is $\tilde{v}_o = 30 \ cm \ s^{-1}$, while arterial diameter is about 0.3 cm; blood dynamic viscosity is $\mu = 0.04 \ g \ cm^{-1} \ s^{-1}$, blood density $\rho = 1 \ g \ cm^{-3}$, thus yielding a kynematic viscosity $\nu = \mu/\rho = 0.04 \ cm^2 \ s^{-1}$ and a Reynolds number $Re = \tilde{v}_o D/\nu$ of order 10^2.

Since we are interested in minimizing blood vorticity in the down-field zone of the bypass, we consider a distributed observation of the vorticity $\nabla \times \mathbf{v}_o$ on a subset $\Omega_o^{df} \subset \Omega_o$; we thus control the system by minimizing the following functional:

$$\mathcal{J}_o(\Omega_o, \mathbf{v}_o) = \frac{\kappa}{2} \int_{\Omega_o^{df}} |\nabla \times \mathbf{v}_o|^2 d\Omega_o, \tag{2}$$

depending both on the shape of the domain Ω_o and on the velocity $\mathbf{v}_o$ that is the solution of the state equation (1); $\kappa > 0$ is a given coefficient. We thus have the following shape optimization problem:

$$\text{find } \hat{\Omega}_o = \arg \min_{\Omega_o \in \mathcal{O}_{ad}} \mathcal{J}_o(\Omega_o, \mathbf{v}_o) \tag{3}$$

where $\mathcal{J}_o(\Omega_o, \mathbf{v}_o)$ is given by (2) and $\mathcal{O}_{ad}$ is a family of admissible shapes. Existence of solutions of this problem is in general stated [29, 33] for

$$\mathcal{O}_{ad} = \{\Omega_o \in \mathcal{U}_L : |\Omega_o| \leq V, \ \overline{\Omega}_o \cap D = \Gamma_{in}\},$$

where $\mathcal{U}_L = \{\Omega_o \subset D, \Omega_o \text{ open Lipschitz domain}\}$ and D is a given fixed rectangle of area V; first order necessary conditions can be derived by either introducing a suitable adjoint problem [39, 14, 13] or using the approach based on Lagrange multipliers [28].

4.2 Parametrized formulation

Indicating with $X(\Omega_o)$ and $Q(\Omega_o)$ the spaces $(H^1_{0,\Gamma_D}(\Omega_o))^2$ and $L^2(\Omega_o)$ respectively, where $H^1_{0,\Gamma_D}(\Omega) = \{v \in H^1(\Omega) : v|_{\Gamma_D} = 0\}$, let us introduce a lift function $R_o \mathbf{g}^D \in (H^1(\Omega_o))^2$ such that $R_o \mathbf{g}^D|_{\Gamma_{in}} = \mathbf{g}_o^D$. We denote $\tilde{\mathbf{v}}_o = \mathbf{v}_o - R_o \mathbf{g}^D$, so that $\tilde{\mathbf{v}}_o|_{\Gamma_D} = \mathbf{0}$ and $\nabla \tilde{\mathbf{v}}_o = \nabla \mathbf{v}_o - \nabla R_o \mathbf{g}^D$. For the sake of simplicity, we still

denote $\tilde{\mathbf{v}}_o$ with $\mathbf{v}_o$ in the sequel, as no ambiguity occurs. The weak formulation of (1) on Ω_o reads as follows: find $(\mathbf{v}_o, p_o) \in X(\Omega_o) \times Q(\Omega_o)$ such that

$$\begin{cases} a^o(\mathbf{v}_o, \boldsymbol{\Phi}) + b^o(p_o, \boldsymbol{\Phi}) = F^o(\boldsymbol{\Phi}) & \forall \ \boldsymbol{\Phi} \in X(\Omega_o) \\ b^o(\varphi, \mathbf{v}_o) = G^o(\varphi) & \forall \ \varphi \in Q(\Omega_o), \end{cases} \tag{4}$$

where, for $1 \le i, j \le d = 2$ (with the implied summation of repeated indices),

$$a^o(\mathbf{v}, \mathbf{w}) = \int_{\Omega_o} \frac{\partial \mathbf{v}}{\partial x_{oi}} \nu_{ij}^o \frac{\partial \mathbf{w}}{\partial x_{oj}} d\Omega_o, \qquad b^o(p, \mathbf{w}) = -\int_{\Omega_o} p\nabla \cdot \mathbf{w} d\Omega_o,$$

$$F^o(\mathbf{w}) = F_f^o(\mathbf{w}) + F_0^o(\mathbf{w}),$$

being $\nu_{ij}^o = \nu\delta_{ij}$, with δ_{ij} indicating the Kronecker symbol. The force field term and the ones due to non-homogeneous Dirichlet boundary conditions are given, respectively, by

$$F_f^o(\mathbf{w}) = \int_{\Omega_o} \mathbf{f}_o \cdot \mathbf{w} d\Omega_o + \int_{\Gamma_{out}^o} \mathbf{g}^N \cdot \mathbf{w} d\Gamma_o,$$

$$F_0^o(\mathbf{w}) = -a^o(R_o\mathbf{g}^D, \mathbf{w}), \qquad G^o(q) = -b^o(q, R_o\mathbf{g}^D).$$

By tracing (4) back on the reference domain Ω by the parametric mapping such that $\Omega_o(\boldsymbol{\mu}) = T(\Omega; \boldsymbol{\mu})$ (whose construction will be discussed in Sec. 5) we have the following parametrized formulation: find $(\mathbf{v}(\boldsymbol{\mu}), p(\boldsymbol{\mu})) \in X(\Omega) \times Q(\Omega)$ such that

$$\begin{cases} a(\mathbf{v}(\boldsymbol{\mu}), \boldsymbol{\Phi}; \boldsymbol{\mu}) + b(p(\boldsymbol{\mu}), \boldsymbol{\Phi}; \boldsymbol{\mu}) = F(\boldsymbol{\Phi}; \boldsymbol{\mu}) & \forall \ \boldsymbol{\Phi} \in X(\Omega) \\ b(\phi, \mathbf{v}(\boldsymbol{\mu}); \boldsymbol{\mu}) = G(\phi; \boldsymbol{\mu}) & \forall \ \phi \in Q(\Omega), \end{cases} \tag{5}$$

where

$$a(\mathbf{v}, \mathbf{w}; \boldsymbol{\mu}) = \int_\Omega \frac{\partial \mathbf{v}}{\partial x_i} \nu_{ij}(\mathbf{x}, \boldsymbol{\mu}) \frac{\partial \mathbf{w}}{\partial x_j} d\Omega, \qquad b(p, \mathbf{w}; \boldsymbol{\mu}) = -\int_\Omega p\chi_{ij}(\mathbf{x}, \boldsymbol{\mu}) \frac{\partial w_j}{\partial x_i} d\Omega,$$

and

$$F(\mathbf{w}; \boldsymbol{\mu}) = F_s(\mathbf{w}; \boldsymbol{\mu}) + F_0(\mathbf{w}; \boldsymbol{\mu}),$$

with

$$F_s(\mathbf{w}; \boldsymbol{\mu}) = \int_\Omega \mathbf{f} \cdot \mathbf{w} \ |\det(\boldsymbol{J}_T)| d\Omega + \int_{\Gamma_{out}} \mathbf{g}^N \cdot \mathbf{w} |\boldsymbol{J}_T \mathbf{t}| d\Gamma,$$

$$F_0(\mathbf{w}; \boldsymbol{\mu}) = -a(R\mathbf{g}^D, \mathbf{w}; \boldsymbol{\mu}), \qquad G(q; \boldsymbol{\mu}) = -b(q, R\mathbf{g}^D; \boldsymbol{\mu}).$$

Notations are as follows:

- $R\mathbf{g}^D \in (H^1(\Omega))^2$ is such that $R\mathbf{g}^D|_{\Gamma_D} = \mathbf{g}^D$ and $\mathbf{t}$ denotes the unit tangential vector to $\partial\Omega$;

- the transformation tensor in the bilinear form $a(\cdot, \cdot; \boldsymbol{\mu})$ is defined as

$$\boldsymbol{\nu}(\mathbf{x}, \boldsymbol{\mu}) = \boldsymbol{J}_T^{-1} \boldsymbol{\nu}^o \boldsymbol{J}_T^{-T} |\det(\boldsymbol{J}_T)|; \tag{6}$$

- the tensor used in the bilinear form $b(\cdot, \cdot; \boldsymbol{\mu})$ is given by

$$\boldsymbol{\chi}(\mathbf{x}, \boldsymbol{\mu}) = \boldsymbol{J}_T^{-1} |\det(\boldsymbol{J}_T)|, \tag{7}$$

where $\boldsymbol{J}_T = \boldsymbol{J}_T(\mathbf{x}, \boldsymbol{\mu})$ denotes the Jacobian of $T(\mathbf{x}, \boldsymbol{\mu})$ and $\det(\boldsymbol{J}_T)$ its determinant.

A necessary condition for the well-posedness of problem (5) is the Babuška "inf-sup" condition [40], which can be stated as follows. Let us introduce $Y := Y(\Omega) = X(\Omega) \times Q(\Omega)$, $\mathbf{V} = (\mathbf{v}, p)^T$ and $\mathbf{W} = (\mathbf{w}, q)^T$; clearly $\|\mathbf{V}\|_Y := \|\mathbf{v}\|_X + \|p\|_Q$ is a norm on the product space Y. Moreover, we can define the bilinear form $\tilde{a}(\cdot; \cdot; \boldsymbol{\mu}) : Y(\Omega) \times Y(\Omega) \to \mathbb{R}$ given by

$$\tilde{a}(\mathbf{V}, \mathbf{W}; \boldsymbol{\mu}) := a(\mathbf{v}; \mathbf{w}; \boldsymbol{\mu}) + b(p, \mathbf{w}; \boldsymbol{\mu}) + b(q, \mathbf{v}; \boldsymbol{\mu}).$$

We next introduce the *supremizer operator* [40] $T^{\boldsymbol{\mu}} : Y \to Y$ such that, for any $\mathbf{W} \in Y$,

$$(T^{\boldsymbol{\mu}} \mathbf{W}, \mathbf{V})_Y = \tilde{a}(\mathbf{W}, \mathbf{V}; \boldsymbol{\mu}), \qquad \forall\, \mathbf{V} \in Y \tag{8}$$

and indicate with $\beta(\boldsymbol{\mu})$ the following quantity,

$$\beta(\boldsymbol{\mu}) := \inf_{\mathbf{W} \in Y} \sup_{\mathbf{V} \in Y} \frac{\tilde{a}(\mathbf{W}, \mathbf{V}; \boldsymbol{\mu})}{\|\mathbf{W}\|_Y \|\mathbf{V}\|_Y}, \tag{9}$$

so that

$$\beta(\boldsymbol{\mu}) \|\mathbf{W}\|_Y \|T^{\boldsymbol{\mu}} \mathbf{W}\|_Y \leq \tilde{a}(\mathbf{W}, T^{\boldsymbol{\mu}} \mathbf{W}; \boldsymbol{\mu}), \qquad \forall\, \mathbf{W} \in Y. \tag{10}$$

Hence, we require that the Babuška "inf-sup" stability condition holds, i.e.

$$\exists\, \beta_0 > 0 : \quad \beta(\boldsymbol{\mu}) \geq \beta_0 > 0, \qquad \forall\, \boldsymbol{\mu} \in \mathcal{D}, \tag{11}$$

where β_0 is said "inf-sup" stability constant. Moreover, we require that the bilinear form $\tilde{a}(\cdot; \cdot; \boldsymbol{\mu})$ is continuous, i.e. the continuity constant

$$\gamma(\boldsymbol{\mu}) := \sup_{\mathbf{V} \in Y} \sup_{\mathbf{W} \in Y} \frac{\tilde{a}(\mathbf{V}, \mathbf{W}; \boldsymbol{\mu})}{\|\mathbf{W}\|_Y \|\mathbf{V}\|_Y}$$

is finite for all $\boldsymbol{\mu} \in \mathcal{D}$, as well as the linear forms $F(\cdot; \boldsymbol{\mu})$ and $G(\cdot; \boldsymbol{\mu})$ are continuous for all $\boldsymbol{\mu} \in \mathcal{D}$. All these hypotheses are verified whether $\nu_{ij}(\cdot; \boldsymbol{\mu}) \in L^{\infty}(\Omega)$, $\chi_{ij}(\cdot; \boldsymbol{\mu}) \in L^{\infty}(\Omega)$ for all $\boldsymbol{\mu} \in \mathcal{D}$ and $\mathbf{f} \in (L^2(\Omega))^2$, $\mathbf{g}^D \in (L^2(\Gamma_D))^2$, $\mathbf{g}^N \in (L^2(\Gamma_N))^2$.

Concerning the minimization problem (3), its parametrized form can be stated as follows:

$$\text{find } \hat{\boldsymbol{\mu}} = \arg\min_{\boldsymbol{\mu} \in \mathcal{D}} s(\boldsymbol{\mu}) \tag{12}$$

where

$$s(\boldsymbol{\mu}) := J(\mathbf{v}(\boldsymbol{\mu})) = \frac{\kappa}{2} \int_{\Omega^{df}} |\mathcal{R}(\mathbf{v}(\boldsymbol{\mu}))|^2 |\det(\boldsymbol{J}_T)| d\Omega, \tag{13}$$

and $\mathcal{R}(\mathbf{v}(\boldsymbol{\mu})) = (\nabla \times \mathbf{v}(\boldsymbol{\mu})) \circ T(\cdot\,; \boldsymbol{\mu}) = (J_T^{-1})_{1j} \partial v_2(\boldsymbol{\mu}) / \partial x_j - (J_T^{-1})_{2j} \partial v_1(\boldsymbol{\mu}) / \partial x_j$, being $(\mathbf{v}(\boldsymbol{\mu}), p(\boldsymbol{\mu}))$ the solution of the parametrized Stokes problem (5). Well posedness and optimality conditions for (12) can be easily derived using standard arguments and techniques [1].

5 Shape parametrization by free-form deformation techniques

Since shape representation is highly specific problem-dependent, various methods have been proposed; a classical approach largely adopted in *geometrical shape optimization* is the so-called *local boundary variation* technique [1, 4], while the most common shape representation adopted in *parametric shape optimization* problems is the explicit *boundary shape parametrization* [41, 35, 34]. The former uses the discrete nodes of the triangulation lying on the boundary as design variables and their displacement for the shape deformation. Since very fine meshes are needed for complex shapes or flows, the number of design variables may become very large, leading to very high computational costs. The latter involves shapes families (mainly polynomial or *spline* functions) depending on a small set of control points, even if a larger number of parameters may be required to represent complex shapes. Nevertheless, after each shape deformation, remeshing is in order.

An alternative approach, potentially able to avoid both problems of complex shapes and remeshing, is the free-form deformation (FFD) technique, in which it is the deformation of an initial design (and not the geometry itself) to be parametrized. The technique consists of embedding the shape to be deformed inside a control area and then of modifying – by acting on a lattice of control points – the metrics of this space and thus the shape within it, rather than in modifying the shape directly. A modification of the control points position thus results in a deformation inside the control area and, automatically, of the computational finite element mesh. Based on tensor product of splines, FFD inherits from boundary parametrization techniques the possibility to handle with global deformations by acting on a small set of control points [5, 6], but provides an easier tool since any explicit parametrization is required [3]. FFD coupled with reduced basis methods has previously been proposed as a parametrization technique for inverse airfoils design [42] and thermal flows control [43]; extensions to three-dimensional geometries is quite straightforward [36].

Given a fixed rectangular domain D containing the reference domain $\Omega \subset D$, we introduce an affine map $\hat{\mathbf{x}} = \Psi(\mathbf{x})$, $\mathbf{x} \in D$, such that $\Psi(D) = (0,1)^2 \equiv \hat{D}$; by this *freezing* procedure, FFD can be defined in a simpler way in the coordinates $\hat{\mathbf{x}} = (\hat{x}_1, \hat{x}_2)$ of the spline parameter space $(0,1)^2$. On $\hat{D}$ we thus select an ordered mesh of $(L+1) \times (M+1)$ unperturbed control points

$$\mathbf{P}_{l,m} = [l/L, m/M]^T, \qquad l = 0, \ldots, L, \quad m = 0, \ldots, M$$

and modify the object by moving a control point to a new position. The corresponding perturbed control points $\mathbf{P}^o_{l,m}$ are thus specified by a set of $(L+1)(M+1)$ parameter vectors $\boldsymbol{\mu}_{l,m} \in \mathbb{R}^2$

$$\mathbf{P}^o_{l,m}(\boldsymbol{\mu}_{l,m}) = \mathbf{P}_{l,m} + \boldsymbol{\mu}_{l,m}, \tag{14}$$

giving in all $2(L+1)(M+1)$ possible degrees of freedom. As often as not, only small subsets of these are selected as design variables if we want to perform a sensible geometrical model order reduction; moreover, several rows or columns of control points can be fixed to obtain desired levels of continuity or to "anchor" certain parts of the domain. In general, among the control points $\mathbf{P}_{l,m}$, we indicate the effectively free scalar-valued parameters chosen as design variables as $\mu_1, \ldots, \mu_P$ – each corresponding to the displacement of a control point in either the $\hat{x}_1$ or the $\hat{x}_2$ direction, i.e. to one of the components of a vector $\boldsymbol{\mu}_{l,m}$ – and define the parametric map $\hat{T}(\cdot; \boldsymbol{\mu}) : \hat{D} \rightarrow \hat{D}_o(\boldsymbol{\mu})$ by which the uploaded geometry is computed as follows:

$$\hat{T}(\hat{\mathbf{x}}; \boldsymbol{\mu}) = \left(\sum_{l=0}^{L} \sum_{m=0}^{M} b_{l,m}^{L,M}(\hat{\mathbf{x}}) \mathbf{P}_{l,m}^{o}(\boldsymbol{\mu}_{l,m}) \right), \tag{15}$$

where

$$b_{l,m}^{L,M}(\hat{\mathbf{x}}) = b_l^L(\hat{x}_1) b_m^M(\hat{x}_2) = \binom{L}{l}\binom{M}{m}(1-\hat{x}_1)^{L-l}\hat{x}_1^l(1-\hat{x}_2)^{M-m}\hat{x}_2^m$$

are tensor products of the unidimensional *Bernstein basis polynomials* defined on $\hat{D}$ by

$$b_l^L(\hat{x}_1) = \binom{L}{l}\hat{x}_1^l(1-\hat{x}_1)^{L-l}, \qquad b_m^M(\hat{x}_2) = \binom{M}{m}\hat{x}_2^m(1-\hat{x}_2)^{M-m}.$$

Finally, the FFD mapping $T(\cdot, \boldsymbol{\mu})$ is obtained as the composition

$$T(\cdot; \boldsymbol{\mu}) : D \rightarrow D_o(\boldsymbol{\mu}), \qquad T(\mathbf{x}; \boldsymbol{\mu}) = \Psi^{-1} \circ \hat{T} \circ \Psi(\mathbf{x}; \boldsymbol{\mu}); \tag{16}$$

in particular, the parametrized domain $\Omega_o(\boldsymbol{\mu})$ is obtained as $\Omega_o(\boldsymbol{\mu}) = \Psi^{-1} \circ \hat{T} \circ \Psi(\Omega; \boldsymbol{\mu})$; see Fig. 4 for a representation of the mapping construction. Since only the degrees of freedom corresponding to $\mu_1, \ldots, \mu_P$ are considered as design variables, the map (15) can be seen as a function of $\boldsymbol{\mu} = (\mu_1 \ldots, \mu_P)$; nevertheless, also other control points – which do not correspond to effective design variables – obviously go under displacement. The number and position of control points chosen have a deep impact on FFD flexibility: it is crucial to maximize the influence of the control points by placing them close to the sensitive regions of the configuration. In particular, displacement of the points belonging to a side on ∂D depends only on the perturbation μ_i of the control points lying on that side, thanks to the expression of the map (15). Using the inverse of $T(\cdot; \boldsymbol{\mu})$ we can get the parametrized formulation of the problem (5) by mapping the equations back onto the reference domain Ω and computing the transformation tensors (6) and (7). Compared to classical strategies such as boundary shape parametrization, FFD techniques lead to low-dimensional parametrizations without loss of accuracy, since perturbations on parameters yield smooth shape deformations even if control points are not related to the shape boundary. Moreover, FFD inherits
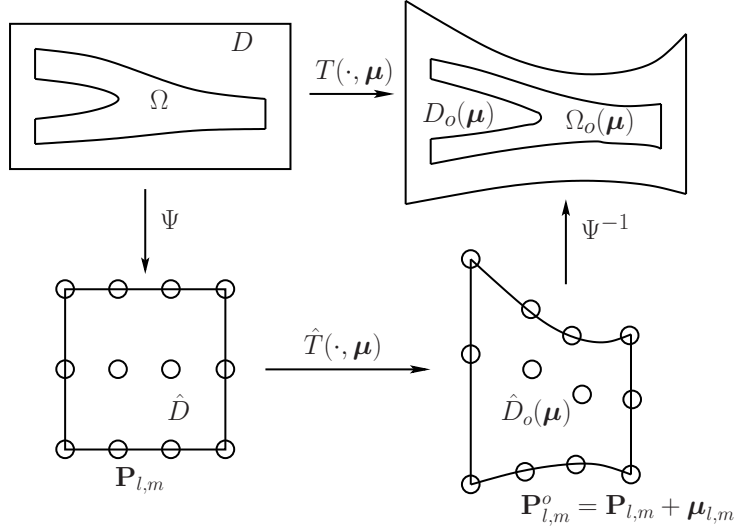
Figure 4: Schematic diagram of the FFD technique: unperturbed control points $\mathbf{P}_{l,m}$, perturbed control points $\mathbf{P}^o_{l,m}(\boldsymbol{\mu}_{l,m})$, mappings $\hat{\mathbf{x}} = \Psi(\mathbf{x})$, $\hat{T}(\hat{\mathbf{x}}; \boldsymbol{\mu})$ and resulting FFD mapping $T(\mathbf{x}; \boldsymbol{\mu}) = (\Psi^{-1} \circ \hat{T} \circ \Psi)(\mathbf{x}; \boldsymbol{\mu})$.

from boundary parametrization techniques the possibility to handle with global deformations by acting on a small set of control points [5, 6], but provides an easier tool since any explicit parametrization is required [3]. We next introduce reduced basis methods for approximating in a rapid and reliable way solutions to (5) and then evaluating the parametric output (13).

6 Reduced basis method for noncoercive PDEs

Our approach to shape optimization takes advantage of *reduced basis* (RB) method for rapid and reliable prediction of engineering outputs associated with PDEs driven by one or more parameters that can represent both physical and geometrical problem features [8, 9]. This method is premised upon a classical finite element (FE) method "truth" approximation space of (typically very large) dimension $\mathcal{N}$ and is based on the use of "snapshot" FE solutions of the PDEs (corresponding to certain values of the parameters) as global approximation basis functions previously computed and stored. Here we are interested in solving by RB method an optimization problem like (5)-(13).

Given two FE spaces $X^{\mathcal{N}}$ and $Q^{\mathcal{N}}$ for velocity and pressure respectively, standard FE discretization of (5) is obtained through a Galerkin projection as follows: find $(\mathbf{v}^{\mathcal{N}}(\boldsymbol{\mu}), p^{\mathcal{N}}(\boldsymbol{\mu})) \in X^{\mathcal{N}} \times Q^{\mathcal{N}}$ such that

$$\begin{cases} a(\mathbf{v}^{\mathcal{N}}(\boldsymbol{\mu}), \boldsymbol{\Phi}; \boldsymbol{\mu}) + b(p^{\mathcal{N}}(\boldsymbol{\mu}), \boldsymbol{\Phi}; \boldsymbol{\mu}) = F(\boldsymbol{\Phi}; \boldsymbol{\mu}) & \forall\, \boldsymbol{\Phi} \in X^{\mathcal{N}} \subset X(\Omega) \\ b(\phi, \mathbf{v}^{\mathcal{N}}(\boldsymbol{\mu}); \boldsymbol{\mu}) = G(\phi; \boldsymbol{\mu}) & \forall\, \phi \in Q^{\mathcal{N}} \subset Q(\Omega). \end{cases} \quad (17)$$

14

The dimension $\mathcal{N} = \mathcal{N}_X + \mathcal{N}_Q$ of the FE spaces is thus taken large enough in order to neglect the differences $\|\mathbf{v}^{\mathcal{N}}(\boldsymbol{\mu}) - \mathbf{v}(\boldsymbol{\mu})\|_{X(\Omega)}$ and $\|p^{\mathcal{N}}(\boldsymbol{\mu}) - p(\boldsymbol{\mu})\|_{Q(\Omega)}$, so that it can be effectively considered as a "truth" approximation. In our case $X^{\mathcal{N}} \times Q^{\mathcal{N}}$ is the space of Taylor-Hood $\mathbb{P}_2 - \mathbb{P}_1$ elements for velocity and pressure, respectively. However, this choice is not restrictive, the whole construction keeps holding for other spaces combinations as well.

6.1 Reduced basis approximation: formulation and main features

The RB method efficienly computes an approximation of $(\mathbf{v}^{\mathcal{N}}(\boldsymbol{\mu}), p^{\mathcal{N}}(\boldsymbol{\mu}))$ by using global approximation spaces made up of well-chosen solutions of (17), i.e. corresponding to specific choices of the parameter values. The basic assumption is that the solution to (5) depends smoothly on the parameters, whence the parametric manifold of solutions in $X(\Omega) \times Q(\Omega)$ is smooth too and can be approximated by selecting, among classical FE solutions, some "snapshot" solutions. Let us take a relatively small set of parameter values $S_N = \{\boldsymbol{\mu}^1, \ldots, \boldsymbol{\mu}^N\}$ and consider the corresponding FE solutions $(\mathbf{v}^{\mathcal{N}}(\boldsymbol{\mu}^1), p^{\mathcal{N}}(\boldsymbol{\mu}^1)), \ldots, (\mathbf{v}^{\mathcal{N}}(\boldsymbol{\mu}^N), p^{\mathcal{N}}(\boldsymbol{\mu}^N))$, where typically $N \ll \mathcal{N}$. We define the *reduced basis pressure space* $Q_N^{\mathcal{N}} \subset Q^{\mathcal{N}}$ as

$$Q_N^{\mathcal{N}} = \operatorname{span}\{\tilde{\zeta}_n := p^{\mathcal{N}}(\boldsymbol{\mu}^n), \ n = 1, \ldots, N\}.$$

The *reduced basis velocity space* $X_N^{\mathcal{N}} \subset X^{\mathcal{N}}$ can be built as

$$X_N^{\mathcal{N}} = \operatorname{span}\{\tilde{\sigma}_n := \mathbf{v}^{\mathcal{N}}(\boldsymbol{\mu}^n), \ T_p^{\boldsymbol{\mu}}\tilde{\zeta}_n, \ n = 1, \ldots, N\},$$

where $T_p^{\boldsymbol{\mu}} : Q_N^{\mathcal{N}} \to X_N^{\mathcal{N}}$ is the so-called *inner supremizer operator* acting on pressure term, defined as

$$(T_p^{\boldsymbol{\mu}}q, \mathbf{w})_X = b(q, \mathbf{w}; \boldsymbol{\mu}) \quad \forall\, \mathbf{w} \in X_N^{\mathcal{N}}. \tag{18}$$

With the above definitions of the two reduced basis spaces, the following LBB condition [13, 17] holds:

$$\inf_{q \in Q_N^{\mathcal{N}}} \sup_{\mathbf{w} \in X_N^{\mathcal{N}}} \frac{b(q, \mathbf{w}; \boldsymbol{\mu})}{\|\mathbf{w}\|_X \|q\|_Q} =: \beta_N(\boldsymbol{\mu}) \geq \beta(\boldsymbol{\mu}) \geq \beta_0 > 0, \qquad \forall\, \boldsymbol{\mu} \in \mathcal{D}. \tag{19}$$

where $\beta(\boldsymbol{\mu})$ and β_0 are the same constants as in (9) and (11). By using Galerkin projection onto $X_N^{\mathcal{N}} \times Q_N^{\mathcal{N}}$ we obtain the following reduced basis approximation: find $(\mathbf{v}_N^{\mathcal{N}}(\boldsymbol{\mu}), p_N^{\mathcal{N}}(\boldsymbol{\mu})) \in X_N^{\mathcal{N}} \times Q_N^{\mathcal{N}}$ such that

$$\begin{cases} a(\mathbf{v}_N^{\mathcal{N}}(\boldsymbol{\mu}), \mathbf{w}; \boldsymbol{\mu}) + b(p_N^{\mathcal{N}}(\boldsymbol{\mu}), \mathbf{w}; \boldsymbol{\mu}) = F(\mathbf{w}; \boldsymbol{\mu}) & \forall\, \mathbf{w} \in X_N^{\mathcal{N}} \\ b(q, \mathbf{v}_N^{\mathcal{N}}(\boldsymbol{\mu}); \boldsymbol{\mu}) = G(q; \boldsymbol{\mu}) & \forall\, q \in Q_N^{\mathcal{N}}. \end{cases} \tag{20}$$

Condition (19) ensures well-posedness of (20). In practice, the Gram-Schmidt orthonormalization procedure [13] has to be adopted, to build basis for pressure

and velocity RB spaces that guarantee algebraic stability (i.e. the condition number of the resulting RB system is relatively small); hence, the RB solution can be written as

$$\mathbf{v}_N^{\mathcal{N}}(\boldsymbol{\mu}) = \sum_{j=1}^{2N} v_{Nj}(\boldsymbol{\mu})\sigma_j, \qquad p_N^{\mathcal{N}}(\boldsymbol{\mu}) = \sum_{l=1}^{N} p_{Nl}(\boldsymbol{\mu})\zeta_l, \qquad (21)$$

where $\{\sigma_j\}_{j=1}^{2N}$ and $\{\zeta_l\}_{l=1}^{N}$ are orthonormal basis for $X_N^{\mathcal{N}}$ and $Q_N^{\mathcal{N}}$, respectively. Since $N \ll \mathcal{N}$, problem (20) has a much lower dimension than (17). RB method offers the possibility to provide both reliable results and rapid response in the real-time and multi-query contexts. Reliability is ensured by rigorous a posteriori estimations [12, 8, 9] for the error in the reduced basis approximation relative to the "truth" FE discretization; rapid response is ensured by an Offline–Online computational strategy that minimizes marginal cost and a rapidly convergent global RB approximation space construction [9]. In this way, in an expensive Offline stage we prepare a very small RB "database", while in the Online stage, for each new value of $\boldsymbol{\mu} \in \mathcal{D}$, we rapidly evaluate both the output of interest and the associated a posteriori error bound whose complexity is independent of the dimension $\mathcal{N}$ of the "truth" FE approximation space.

6.2 Reduced basis space assembling and error estimation

The choice of the snapshot solutions is crucial for the accuracy of the RB approximation and is operated using the following *greedy* algorithm [8, 9]. Let $\Xi_{train} \subset \mathcal{D}$ be a (sufficiently rich) finite training sample of parameter points chosen using a uniform distribution on $\mathcal{D}$ and indicate by $\mathbf{V}^{\mathcal{N}}(\boldsymbol{\mu}) = (\mathbf{v}^{\mathcal{N}}(\boldsymbol{\mu}), p^{\mathcal{N}}(\boldsymbol{\mu}))$, $\mathbf{V}_N^{\mathcal{N}}(\boldsymbol{\mu}) = (\mathbf{v}_N^{\mathcal{N}}(\boldsymbol{\mu}), p_N^{\mathcal{N}}(\boldsymbol{\mu}))$ the FE approximation and the RB approximation, respectively (we are using notations for spaces and norms introduced in Sec. 4.2). Given the first parameter value $\boldsymbol{\mu}^1$ and a sharp, rigorous and inexpensive error bound $\Delta_n(\boldsymbol{\mu})$ for the norm such that

$$\|\mathbf{V}^{\mathcal{N}}(\boldsymbol{\mu}) - \mathbf{V}_n^{\mathcal{N}}(\boldsymbol{\mu})\|_Y \leq \Delta_n(\boldsymbol{\mu}) \quad \text{for all } \boldsymbol{\mu} \in \mathcal{D},$$

we choose the remaining parameter values (and corresponding snapshot solutions) as

$$\boldsymbol{\mu}^n := \arg \max_{\boldsymbol{\mu} \in \Xi_{train}} \Delta_{n-1}(\boldsymbol{\mu}), \quad \text{for } n = 2, \dots, N$$

until an error tolerance ε_{tol}^{RB} a priori fixed is achieved:

$$\Delta_N(\boldsymbol{\mu}) \leq \varepsilon_{tol}^{RB} \quad \text{for all } \boldsymbol{\mu} \in \Xi_{train}.$$

The error bound $\Delta_n(\boldsymbol{\mu})$ is also used for estimating the error of the RB approximation w.r.t. the "truth" FE solution [8, 9] and can be defined introducing the residuals

$$r_n^v(\mathbf{w}; \boldsymbol{\mu}) := F(\mathbf{w}; \boldsymbol{\mu}) - a(\mathbf{v}_n^{\mathcal{N}}(\boldsymbol{\mu}), \mathbf{w}; \boldsymbol{\mu}) - b(p_n^{\mathcal{N}}(\boldsymbol{\mu}), \mathbf{w}; \boldsymbol{\mu}),$$
$$r_n^p(q; \boldsymbol{\mu}) := G(q; \boldsymbol{\mu}) - b(q, \mathbf{v}_n^{\mathcal{N}}(\boldsymbol{\mu}); \boldsymbol{\mu}).$$

Note that

$$r_n^v(\mathbf{w}; \boldsymbol{\mu}) = a(\mathbf{v}^{\mathcal{N}}(\boldsymbol{\mu}) - \mathbf{v}_n^{\mathcal{N}}(\boldsymbol{\mu}), \mathbf{w}; \boldsymbol{\mu}) + b(p^{\mathcal{N}}(\boldsymbol{\mu}) - p_n^{\mathcal{N}}(\boldsymbol{\mu}), \mathbf{w}; \boldsymbol{\mu}) \quad \forall\, \mathbf{w} \in X^{\mathcal{N}},$$
$$r_n^p(q; \boldsymbol{\mu}) = b(q, \mathbf{v}^{\mathcal{N}}(\boldsymbol{\mu}) - \mathbf{v}_n^{\mathcal{N}}(\boldsymbol{\mu}); \boldsymbol{\mu}) \quad \forall\, q \in Q^{\mathcal{N}}$$

or, equivalently,

$$\tilde{r}_n(\mathbf{W}; \boldsymbol{\mu}) = \tilde{a}(\mathbf{V}^{\mathcal{N}}(\boldsymbol{\mu}) - \mathbf{V}_n^{\mathcal{N}}(\boldsymbol{\mu}), \mathbf{W}; \boldsymbol{\mu}) \quad \forall\, \mathbf{W} \in Y^{\mathcal{N}} \equiv X^{\mathcal{N}} \times Q^{\mathcal{N}},$$

where $\tilde{r}_n(\mathbf{W}; \boldsymbol{\mu}) := r_n^v(\mathbf{w}; \boldsymbol{\mu}) + r_n^p(q; \boldsymbol{\mu})$. Using the condition (10), we have the following residual-based estimator

$$\|\mathbf{V}^{\mathcal{N}}(\boldsymbol{\mu}) - \mathbf{V}_n^{\mathcal{N}}\|_Y \leq \frac{\|\tilde{r}_n(\cdot; \boldsymbol{\mu})\|_{Y'}}{\beta_{LB}(\boldsymbol{\mu})} =: \Delta_n(\boldsymbol{\mu}) \tag{22}$$

where $\|\cdot\|_{Y'}$ is the dual norm of the residual defined as

$$\|\tilde{r}_n(\cdot; \boldsymbol{\mu})\|_{Y'} = \sup_{\mathbf{V} \in Y^{\mathcal{N}}} \frac{\tilde{r}_n(\mathbf{V}; \boldsymbol{\mu})}{\|\mathbf{V}\|_Y}$$

and $\beta_{LB}(\boldsymbol{\mu})$ is a computable lower bound for the inf-sup constant $\beta(\boldsymbol{\mu})$ [44]. Efficient and reliable methods of computing both the dual norm of the residual and $\beta_{LB}(\boldsymbol{\mu})$ will be reported in a forthcoming work [45]. Once the reduced basis approximation $(\mathbf{v}_N(\boldsymbol{\mu}), p_N(\boldsymbol{\mu}))$ has been computed for a given $\boldsymbol{\mu} \in \mathcal{D}$ by solving the system (20), we are interested in the error estimation with respect to the corresponding FE solution $(\mathbf{v}_N^{\mathcal{N}}(\boldsymbol{\mu}), p_N^{\mathcal{N}}(\boldsymbol{\mu}))$. Since the use of a priori theory proves to be rather difficult in this context, we use the same residual-based estimator (22) in order to provide a posteriori error estimates in a rapid and reliable way. Moreover, a posteriori error estimators for the error on the output $|s^{\mathcal{N}}(\boldsymbol{\mu}) - s_N^{\mathcal{N}}(\boldsymbol{\mu})| = |J(\mathbf{v}^{\mathcal{N}}(\boldsymbol{\mu})) - J(\mathbf{v}_N^{\mathcal{N}}(\boldsymbol{\mu}))|$ (see [46]) could be introduced, but their characterization in the noncoercive case for quadratic outputs is more difficult and is currently under investigation.

6.3 Offline-Online efficient computational strategy

A suitable Offline/Online decomposition stratagem enables to decouple the generation and projection stages of the RB approximation: a very expensive (parameter independent) pre-processing performed Offline once prepares the way for subsequent very inexpensive calculations performed Online for each new PDEs solution or input-output evaluation required. The possibility to handle with this computational procedure is based on an affine parametric dependence assumption on both bilinear and linear forms. If the mapping $T(\cdot; \boldsymbol{\mu}) : \Omega \rightarrow \Omega_o(\boldsymbol{\mu})$ is affine, parametric bilinear forms $a(\cdot, \cdot; \boldsymbol{\mu})$ and $b(\cdot, \cdot; \boldsymbol{\mu})$ are affinely parametrized [9, 8], i.e.

$$a(\mathbf{v}, \mathbf{w}; \boldsymbol{\mu}) = \sum_{q=1}^{Q_a} \Theta_a^q(\boldsymbol{\mu}) a^q(\mathbf{v}, \mathbf{w}), \qquad b(p, \mathbf{w}; \boldsymbol{\mu}) = \sum_{q=1}^{Q_b} \Theta_b^q(\boldsymbol{\mu}) b^q(p, \mathbf{w})$$

for some integers Q_a, Q_b, where q is a condensed index for (i, j, k),

$$a^{q(i,j,k)}(\mathbf{v}, \mathbf{w}) = \int_\Omega \xi_k^{i,j}(\mathbf{x}) \frac{\partial \mathbf{v}}{\partial x_i} \frac{\partial \mathbf{w}}{\partial x_j} d\Omega, \quad b^{q(i,j,k)}(p, \mathbf{w}) = \int_\Omega \eta_k^{i,j}(\mathbf{x}) p \frac{\partial \mathbf{w}_i}{\partial x_j} d\Omega,$$
(23)
$$\Theta_a^q(\boldsymbol{\mu}) = \beta_k^{i,j}(\boldsymbol{\mu}), \qquad \Theta_b^q(\boldsymbol{\mu}) = \gamma_k^{i,j}(\boldsymbol{\mu})$$

and, for $1 \le i, j \le 2$,

$$\nu_{ij}(\mathbf{x}, \boldsymbol{\mu}) = \sum_{k=1}^{K_{ij}^a} \beta_k^{i,j}(\boldsymbol{\mu}) \xi_k^{i,j}(\mathbf{x}), \qquad \chi_{ij}(\mathbf{x}, \boldsymbol{\mu}) = \sum_{k=1}^{K_{ij}^b} \gamma_k^{i,j}(\boldsymbol{\mu}) \eta_k^{i,j}(\mathbf{x}).$$
(24)

In the same way, we can write the right-hand-side terms as

$$F(\mathbf{w}; \boldsymbol{\mu}) = \sum_{q=1}^{Q_F+Q_a} \tilde{\Theta}_q^F(\boldsymbol{\mu}) F^q(\mathbf{w}), \qquad G(\phi; \boldsymbol{\mu}) = \sum_{q=1}^{Q_G} \Theta_q^G(\boldsymbol{\mu}) G^q(\phi)$$

for some integers Q_F and $Q_G \equiv Q_b$, where here q is a condensed index for (i, k),

$$F^q(\mathbf{w}) = \int_\Omega \psi_k^i(\mathbf{x}) \mathbf{w}_i d\Omega, \qquad \Theta_q^F(\boldsymbol{\mu}) = \delta_k^i(\boldsymbol{\mu}), \qquad q = 1, \ldots, Q_F,$$
(25)

$$f_i(\mathbf{x}) |\det J_T(\mathbf{x}, \boldsymbol{\mu})| = \sum_{k=1}^{K_i^f} \delta_k^i(\boldsymbol{\mu}) \psi_k^i(\mathbf{x}), \qquad i = 1, 2,$$
(26)

$$F^q(\mathbf{w}) = a^q(R\mathbf{v}_g, \mathbf{w}), \quad \tilde{\Theta}_q^F(\boldsymbol{\mu}) = -\Theta_q^a(\boldsymbol{\mu}), \qquad q = Q_F + 1, \ldots, Q_F + Q_a,$$
$$G^q(\phi) = b^q(\phi, R\mathbf{v}_g), \quad \tilde{\Theta}_q^G(\boldsymbol{\mu}) = -\Theta_q^b(\boldsymbol{\mu}), \qquad q = 1, \ldots, Q_G = Q_b.$$
(27)

These assumptions enable to split the computation of solutions for (20) into Offline and Online stages, since from (20) we obtain

$$\begin{cases} \displaystyle\sum_{q=1}^{Q_a} \Theta_a^q(\boldsymbol{\mu}) a^q(\mathbf{v}_N^{\mathcal{N}}(\boldsymbol{\mu}), \mathbf{w}) + \sum_{q=1}^{Q_b} \Theta_b^q(\boldsymbol{\mu}) b^q(p_N^{\mathcal{N}}(\boldsymbol{\mu}), \mathbf{w}) = \sum_{q=1}^{Q_F+Q_a} \tilde{\Theta}_q^F(\boldsymbol{\mu}) F^q(\mathbf{w}) \\ \displaystyle\sum_{q=1}^{Q_b} \Theta_b^q(\boldsymbol{\mu}) b^q(q, \mathbf{v}_N^{\mathcal{N}}(\boldsymbol{\mu})) = \sum_{q=1}^{Q_G} \Theta_q^G(\boldsymbol{\mu}) G^q(\phi) \end{cases}$$
(28)

for all $\mathbf{w} \in X_N^{\mathcal{N}}$, $\phi \in Q_N^{\mathcal{N}}$. Using the expressions (21), system (28) becomes, componentwise, for $1 \le i \le 2N$ and $1 \le l \le N$,

$$\begin{cases} \displaystyle\sum_{j=1}^{2N}\sum_{q=1}^{Q_a} \Theta_a^q(\boldsymbol{\mu}) A_{ij}^q v_{Nj}(\boldsymbol{\mu}) + \sum_{l=1}^{N}\sum_{q=1}^{Q_b} \Theta_b^q(\boldsymbol{\mu}) B_{il}^q p_{Nl}(\boldsymbol{\mu}) = \sum_{q=1}^{Q_F+Q_a} \tilde{\Theta}_q^f(\boldsymbol{\mu}) F_i^q, \\ \displaystyle\sum_{j=1}^{2N}\sum_{q=1}^{Q_b} \Theta_b^q(\boldsymbol{\mu}) B_{jl}^q v_{Nj}(\boldsymbol{\mu}) = \sum_{q=1}^{Q_G} \Theta_q^g(\boldsymbol{\mu}) G_l^q, \end{cases}$$
(29)

where $A_{ij}^q = a^q(\sigma_j, \sigma_i)$, $B_{il}^q = b^q(\zeta_l, \sigma_i)$, $F_i^q = \mathbf{f}^q(\sigma_i)$ and $G_l^q = g^q(\zeta_l)$. In this way, computation entails an expensive $\boldsymbol{\mu}$-independent Offline stage performed only once and an Online stage for any chosen parameter value $\boldsymbol{\mu} \in \mathcal{D}$. During the former the basis functions σ_n, ζ_l, the matrices A^q, B^q and the vectors F^q, G^q are computed and stored; in the latter, for any given $\boldsymbol{\mu}$, all the $\Theta_q(\boldsymbol{\mu})$ coefficients are evaluated and then the $3N \times 3N$ linear system (29) is assembled and solved as a usual Stokes system, being of the form

$$\begin{pmatrix} A & B \\ B^T & 0 \end{pmatrix} \begin{pmatrix} v_N \\ p_N \end{pmatrix} = \begin{pmatrix} F \\ G \end{pmatrix}. \tag{30}$$

Although being dense (rather than sparse as in the FE case), the system matrix is very small, with a size independent of the FE space dimension $\mathcal{N}$. Details about the assembling procedure of these matrices will be given in the next section. Moreover, also the dual norm of the residual appearing in (22) can be computed efficiently by using the Offline-Online procedure [8, 9].

Since the map $T(\cdot; \boldsymbol{\mu})$ (15) obtained by FFD method is in general a polynomial map, the tensor $\boldsymbol{\nu}_T(\mathbf{x}; \boldsymbol{\mu})$ is not affinely parametrized in the sense of (24) nor is $|\det(J_T)|$ appearing also in $\boldsymbol{\chi}_T(\mathbf{x}; \boldsymbol{\mu})$ and $\mathbf{F}(\mathbf{w}; \boldsymbol{\mu})$. Hence, an intermediate step is necessary in order to recover the affinity assumption and thus the possibility of computing the RB solution through an Offline/Online decomposition. In the non-affine case, we rely on the empirical interpolation method (EIM) [10, 11], which is an interpolation method for parametric functions based on adaptively chosen interpolation points and global shape functions. According to EIM each component $\nu_{ij}(\mathbf{x}; \boldsymbol{\mu})$ is approximated by an affine expression given by

$$\tilde{\nu}_{i,j}(\mathbf{x}; \boldsymbol{\mu}) = \sum_{k=1}^{K_{ij}^a} \tilde{\beta}_k^{i,j}(\boldsymbol{\mu}) \tilde{\xi}_k^{i,j}(\mathbf{x}) + \varepsilon_{i,j}^a(\mathbf{x}; \boldsymbol{\mu}). \tag{31}$$

The same approximation is set up for the components of the $\boldsymbol{\chi}_T$ tensor and the right-hand-side of velocity equation:

$$\tilde{\chi}_{i,j}(\mathbf{x}; \boldsymbol{\mu}) = \sum_{k=1}^{K_{ij}^b} \tilde{\gamma}_k^{i,j}(\boldsymbol{\mu}) \tilde{\eta}_k^{i,j}(\mathbf{x}) + \varepsilon_{i,j}^b(\mathbf{x}; \boldsymbol{\mu}),$$

$$f_i(\mathbf{x}) |\det(J_T(\mathbf{x}; \boldsymbol{\mu}))| = \sum_{k=1}^{\tilde{K}_i} \tilde{\delta}_k^i(\boldsymbol{\mu}) \tilde{\psi}_m^i(\mathbf{x}) + \varepsilon_i(\mathbf{x}; \boldsymbol{\mu}). \tag{32}$$

All the coefficients $\beta_m^{i,j}$'s, $\gamma_m^{i,j}$'s, δ_m^i's, $\xi_k^{i,j}$'s, $\eta_k^{i,j}$'s and ψ_m^i's are efficiently computable scalar functions and the error terms are guaranteed to be under some tolerance,

$$\|\varepsilon_{i,j}^{(a,b)}(\cdot; \boldsymbol{\mu})\|_\infty \le \varepsilon_{tol}^{EIM}, \quad \|\varepsilon_i(\cdot; \boldsymbol{\mu})\|_\infty \le \varepsilon_{tol}^{EIM}, \quad \forall \boldsymbol{\mu} \in \mathcal{D}.$$

We refer the reader to Barrault et al. [10] and Nguyen [12] for details on EIM procedures for non-affine RB problems and to a more recent work [42] for details on EIM implementation and application in the FFD context introduced in Sec. 5.

7 Numerical solution of parametric shape optimization problems

At this stage, reduced basis methods, combined with shape parametrization by free-form deformation and empirical interpolation for treating non-affinities, enable to solve the parametrized optimization problem (12), which is a nonlinear programming problem but depending on a relatively small number of parameters, in a very efficient way. We proceed as follows. We consider the reduced version of (12):

$$\text{find } \hat{\boldsymbol{\mu}}_N = \arg\min_{\boldsymbol{\mu} \in \mathcal{D}} s_N(\boldsymbol{\mu}) \tag{33}$$

where

$$s_N(\boldsymbol{\mu}) := J_N(\mathbf{v}_N^{\mathcal{N}}(\boldsymbol{\mu})) = \frac{\kappa}{2} \int_{\Omega^{df}} |\mathcal{R}(\mathbf{v}_N^{\mathcal{N}}(\boldsymbol{\mu}))|^2 |\det(\boldsymbol{J}_T)| d\Omega \tag{34}$$

being $(\mathbf{v}_N^{\mathcal{N}}(\boldsymbol{\mu}), p_N^{\mathcal{N}}(\boldsymbol{\mu}))$ the RB solution to the system (20). Thus, in the Offline stage, we perform once for all parameter-independent computations to set geometrical parametrization and RB structures. In more details:

1. we compute the parametric FFD mapping $T(\cdot; \boldsymbol{\mu})$ (16) and perform the empirical interpolation to obtain the affinely parametrized expansions (24)-(26);

2. we assemble the finite element matrices $\mathcal{A}^q \in \mathbb{R}^{\mathcal{N}_X \times \mathcal{N}_X}$ ($q = 1, \ldots, Q_a$), $\mathcal{B}^q \in \mathbb{R}^{\mathcal{N}_X \times \mathcal{N}_Q}$ ($q = 1, \ldots, Q_b$) corresponding to the bilinear forms (23), the right-hand sides $\mathcal{F}^q \in \mathbb{R}^{\mathcal{N}_X}$ ($q = 1, \ldots, Q_F$), $\mathcal{G}^q \in \mathbb{R}^{\mathcal{N}_Q}$ ($q = 1, \ldots, Q_G$) corresponding to the linear forms (25) and (27);

3. we calculate a lower bound $\beta_{LB}(\boldsymbol{\mu})$ for the inf-sup constant by means of the successive constraint method [44, 9];

4. we perform the *greedy* procedure presented in Sec. 6.2 for building the RB spaces $X_N^{\mathcal{N}}$ and $Q_N^{\mathcal{N}}$ for velocity and pressure respectively. Each Stokes problem has been solved using the *Pressure-Matrix Method*; moreover, at each iteration the space $X_N^{\mathcal{N}}$ is enriched by the solution of (18) (supremizer operator) and a Gram-Schmidt ortonormalization is executed;

5. after the *greedy* basis selection procedure, matrices A^q, B^q and vectors F^q, G^q are obtained by a pre- and post- multiplication of the corresponding FE structures with the RB representations $\mathcal{Z}_X = [\sigma_1 | \ldots | \sigma_{2N}]$, $\mathcal{Z}_Q = [\zeta_1 | \ldots | \zeta_N]$:

$$\begin{aligned} A^q &= \mathcal{Z}_X^T \mathcal{A}^q \mathcal{Z}_X, \quad q = 1, \ldots, Q_a; \qquad B^q = \mathcal{Z}_X^T \mathcal{B}^q \mathcal{Z}_X, \quad q = 1, \ldots, Q_b; \\ F^q &= \mathcal{Z}_X^T \mathcal{F}^q, \quad q = 1, \ldots, Q_a + Q_F; \quad G^q = \mathcal{Z}_Q^T \mathcal{G}^q, \quad q = 1, \ldots, Q_G \equiv Q_b. \end{aligned}$$

The *Offline* stage thus depends on the choice of the FE spaces (whose dimension is $\mathcal{N}_X + \mathcal{N}_Q$), the reference domain Ω and the FFD structure. For the RB Offline computations we have used the `rbMIT` library [47, 8], while for the FE assembling stage we have exploited the `MLife` library [48], enhanced in `Matlab`-PDE toolbox environment.

The *Online* stage consists of many evaluations of field variables $(\mathbf{v}_N^{\mathcal{N}}(\boldsymbol{\mu}), p_N^{\mathcal{N}}(\boldsymbol{\mu}))$ and parametric output $s_N(\boldsymbol{\mu})$, as required by the optimization procedure chosen to solve minimization problem (33); in our case, it has been solved using the sequential quadratic programming (SQP) algorithm, see e.g. [49].

8   Numerical results

Let us now present the results obtained through the parametric optimization framework described in the previous sections. Two different cases have been performed, considering different patencies (i.e. different blockage conditions) in the occluded coronary artery: the presence of a residual blood flow in this vessel impacts on the global behaviour of the flow in the anastomosis, involving different vorticity profiles in the region. In Case A a completely occluded coronary is considered, with $\mathbf{g}^D = \mathbf{0}$ on Γ_a (completed blockage), while in Case B a partially stenosed coronary is considered, choosing a residual horizontal flux given by $\mathbf{g}^D = (\max(\tilde{v}_0 \exp(-(x - x_M)^2/\beta) - \omega, 0), 0)$ on Γ_a, where x_M is the middle point of side Γ_a and $\beta = 10^{-3}$, $\omega = 10^{-1}$ are constants which model the patency of the stenosis; here we consider a residual flow rate of about 15% of the flow rate in the bypass grafting. In both cases, the same reference configuration Ω, depicted in Fig. 5, has been chosen similar to some bypass configurations already considered in previous works [25, 14, 13], fixing the observation subregion $\Omega_{df} = \{\mathbf{x} = (x_1, x_2) \in \Omega : x_1 > 1.5\}$. In each case the FFD configuration used was an array of 5×6 control points on the rectangle $D = [-1, 3] \times [-0.6, 0.4]$, for a total number of 60 degrees of freedom; $P = 8$ of these degrees of freedom have been selected as design variables, seven of which corresponding to perturbation in the vertical direction and one of which allowed to move in the horizontal direction.

Previous analysis on the shape of an aorto-coronaric bypass [19, 20, 13, 27] have highlighted an important dependence of the blood flow on the *anastomotic angle* between the incoming branch of the graft and the artery, and on the ratio between the diameters of this two branches; our selected design variables thus control shape variations in this sense. In particular, the parameters μ_3 and μ_5 (the latter is the only one giving an horizontal deformation) control the anastomotic angle, the parameters μ_6 and μ_8 control the ratio between the diameters of the graft inlet segment and of the host artery (see Fig. 3). Moreover, the parameters μ_4 and μ_7 control the upper shape of the anastomotic bifurcation, while μ_1 and μ_2 are responsible of the shape of the lower wall, which has to be

curved since it is positioned on the heart wall; the fact that the shape of the bottom boundary depends only on these two last parameters allows to control its curvature in a more precise way. The parametric domain $\mathcal{D}$ is therefore given by

$$\mathcal{D} = \{\boldsymbol{\mu} = (\mu_1, \ldots, \mu_8) \in \mathbb{R}^8 : \mu_i \in [-0.2, 0.2] \ \forall \ i \neq 5, \ \mu_5 \in [0, 1]\};$$

details on location of control points and selected design variables are shown in Fig. 5.
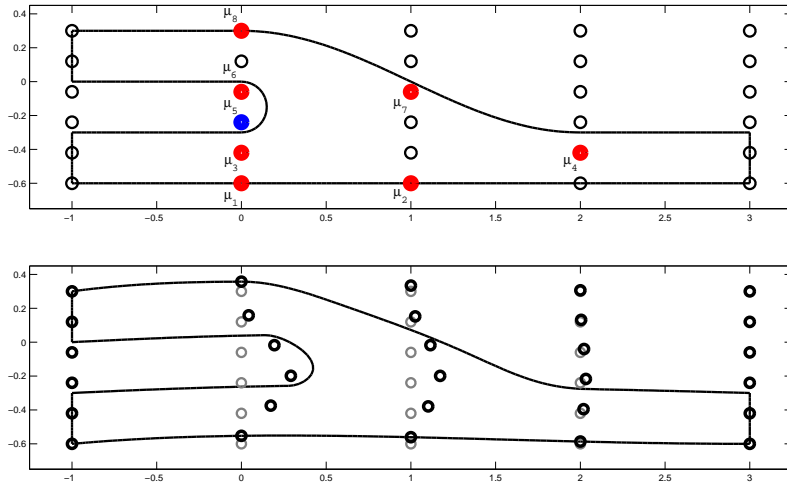
Figure 5: Top: reference domain Ω and free-form deformation setting. Control points depicted in red and blue can be freely moved in vertical or horizontal direction, respectively. Bottom: an example of shape deformation; grey points correspond to the undeformed shape (i.e. $\boldsymbol{\mu} = \mathbf{0}$), while black points correspond to the choice $\boldsymbol{\mu} = (0.1, 0.05, 0.15, 0.1, 0.5, 0.15, 0.2, 0.15)$.

Reduced basis approximation have been built upon a finite element approximation on $\mathbb{P}^2 - \mathbb{P}^1$ spaces of dimension $\mathcal{N}_X = 33,330$ and $\mathcal{N}_Q = 4,269$ respectively, obtained on a non-conforming mesh of $8,128$ triangular elements. In particular, since FFD and EIM steps are independent of the reference configuration, they can be performed only once for both cases A and B. In both cases, the stopping tolerance is $\varepsilon_{tol}^{EIM} = 2.5 \times 10^{-4}$, giving for both cases an affine expansion of $\sum_{i,j} \tilde{K}_{ij}^a = 204$ terms for $\tilde{\nu}_{ij}$ components, of $\sum_{i,j} \tilde{K}_{ij}^b = 18$ terms for $\tilde{\chi}_{ij}$ components and of $\sum_i \tilde{K}_i^f = 5$ terms for the right hand-side components; see Fig. 6 for an example of tensor reconstruction through EIM.

Instead, all the FE structures assembling, the estimation of the lower bound of the inf-sup constant and the *greedy* algorithm for snapshots selection have to be done separately, once for each case. In particular, tolerances for RB *greedy*

algorithm ε_{tol}^{RB} and empirical interpolation ε_{tol}^{EIM} are chosen such that the error on EIM is kept under the error on RB construction; with $\varepsilon_{tol}^{RB} = 5 \cdot 10^{-3}$, $N = 24$ and $N = 22$ basis functions have been selected for case A and B, giving RB spaces of total dimension 72 and 66, respectively.

In Fig. 7 the convergence of the *greedy* algorithm for the RB space construction during the Offline stage is shown, while the selected snapshots $\boldsymbol{\mu}$ are reported in Figs. 8 and 9 for the test cases A and B, respectively. Moreover, a tolerance $\varepsilon_{tol}^{OPT} = 10^{-6}$ has been chosen for the stopping criterium of the optimization procedure, based on the magnitude of the (approximated) gradient of the cost functional.
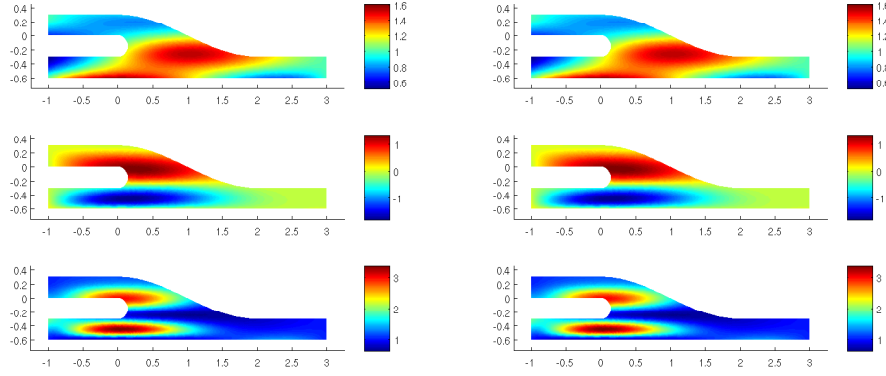
Figure 6: Tensor components $\nu_{1,1}(\mathbf{x}; \bar{\boldsymbol{\mu}})$, $\nu_{1,2}(\mathbf{x}; \bar{\boldsymbol{\mu}}) \equiv \nu_{2,1}(\mathbf{x}; \bar{\boldsymbol{\mu}})$, $\nu_{2,2}(\mathbf{x}; \bar{\boldsymbol{\mu}})$ on Ω for a randomly chosen $\bar{\boldsymbol{\mu}} \in \mathcal{D}$ (left) and corresponding affine reconstructions obtained by empirical interpolation (right).
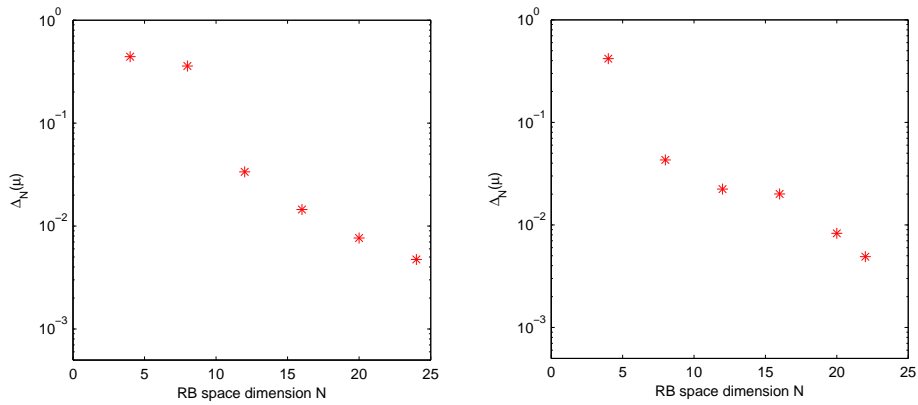
Figure 7: Convergence of the *greedy* algorithm for the RB approximation space construction in test case A (left) and B (right).
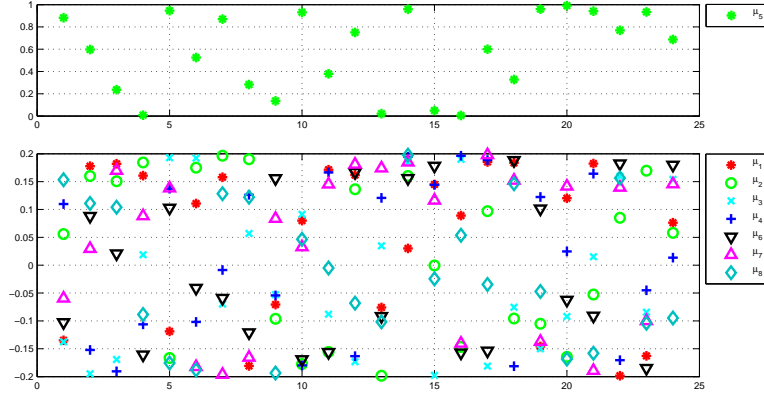
Figure 8: Test case A: parameters distribution during the Offline RB approximation space construction.
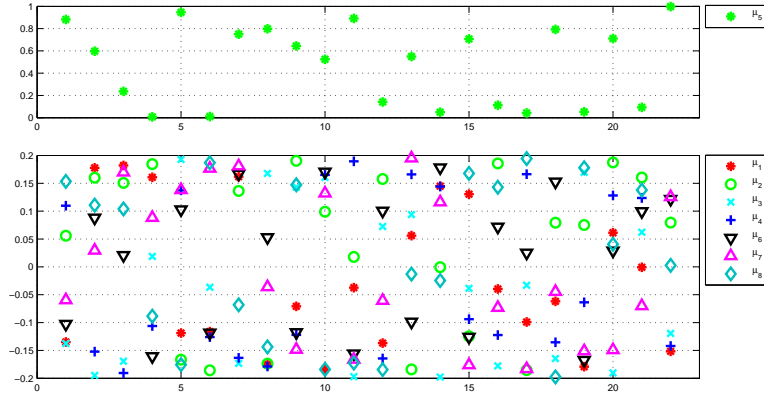
Figure 9: Test case B: parameters distribution during the Offline RB approximation space construction.

8.1 Modelling aspects

For the test case A, a vorticity reduction of about 55% has been obtained through the procedure described above. By choosing $\kappa = 2 \cdot 10^2$, the cost functional decreases from an initial value $s_N(\boldsymbol{\mu}^{(0)}) = 0.680$ to an optimal value $s_N(\hat{\boldsymbol{\mu}}) = 0.301$ after 36 optimization steps performed in $2968s$ until convergence[a].

In Fig. 10 the reference and the optimal configurations are displayed, together with deformation induced by the displacement of the control points. In Fig. 11 velocity and pressure fields for the reference configuration are represented, together with the corresponding vorticity field; flow variables and vorticity field obtained for the optimal configuration are instead represented in Fig. 12.

---

[a]Computations have been executed on a personal computer with 2×2GHz Dual Core AMD Opteron (tm) processors 2214 HE and 16 GB of RAM.
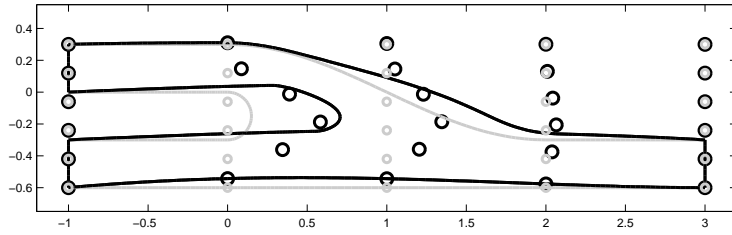
Figure 10: Test A: reference configuration (in grey), optimal shape (in black) and corresponding control points displacement.
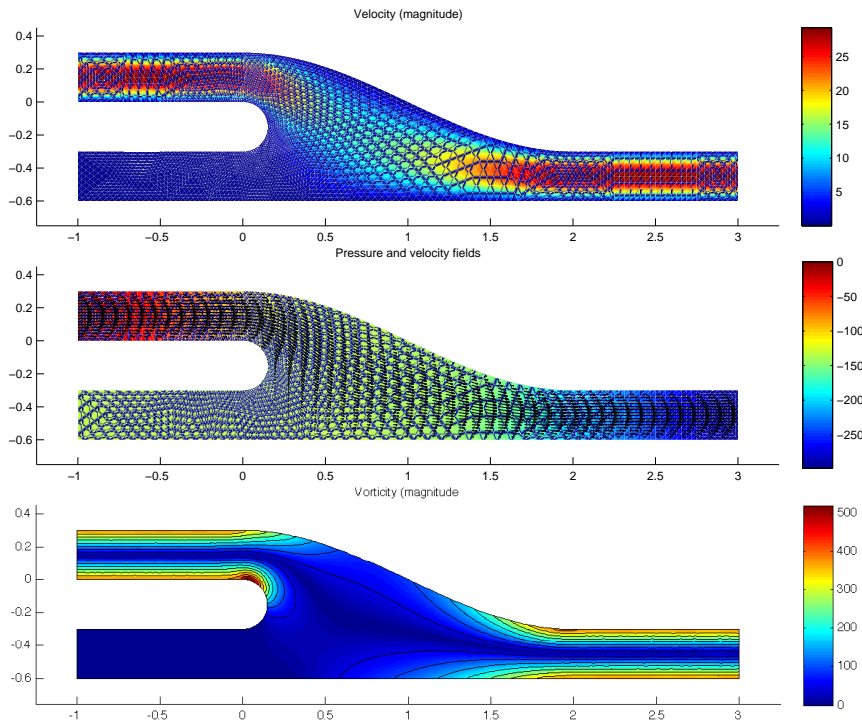
Figure 11: Test A: velocity field, pressure field and vorticity magnitude for the reference configuration.

For the test case B, a vorticity reduction of about 60% has been obtained, passing from an initial value of the cost functional $s_N(\boldsymbol{\mu}^{(0)}) = 1.249$ to an optimal value of $s_N(\hat{\boldsymbol{\mu}}) = 0.458$ after 45 optimization steps, which have been performed in $3554s$. Optimal configuration obtained in this case is displaied in Fig. 13, while flow variables and the corresponding vorticity pattern for the initial and the optimal configurations are represented in Figs. 14 and 15.

The results of the analysis performed in this work show that graft anastomosis configurations play an important role in the pattern of the flow and the distribution of the vorticity generated downstream. A remarkable observation is that – even if the optimal shape are quite similar – the magnitude of the vor-
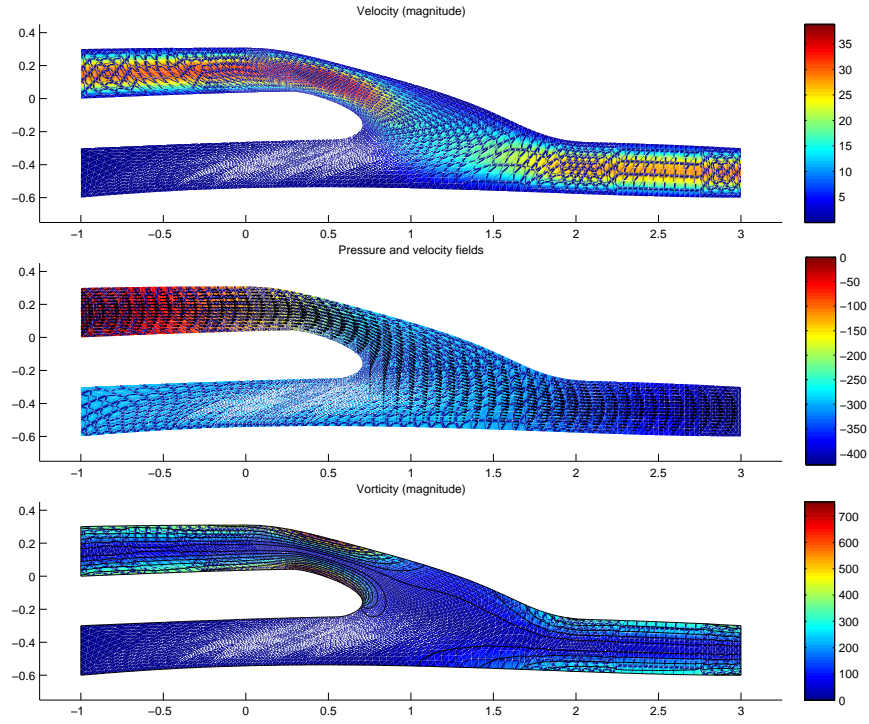
Figure 12: Test A: velocity field, pressure field and vorticity magnitude for the optimal configuration.
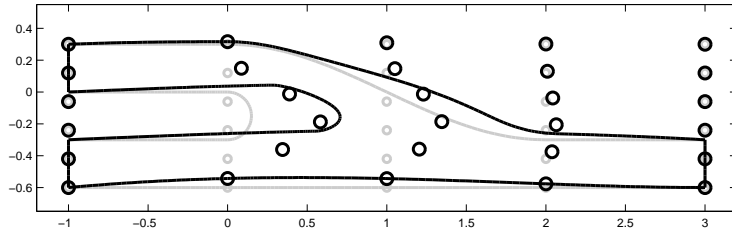
Figure 13: Test B: reference configuration and optimal shape with corresponding control points displacement.

ticity on the anastomosis highly depends on the presence of a residual patency in the obstructed host coronary artery; in particular, in the down field region vorticity magnitude is higher whether a residual flow is present. In both cases, the iteratively optimized geometry has a much smoother toe and heel than the initial shape; optimal shapes also show smoother curvatures at the heel with a gradual transition in the toe region, as already pointed out in the work by Lei et al. [25]. The localization of maximum values of vorticity at the heel and toe is expected, because this is the region where disturbed flows occur, even with a Stokes model; the same conclusion can be drawn for wall shear stress gradient and Navier-Stokes flows [25]. Moreover, higher values in the heel region are not
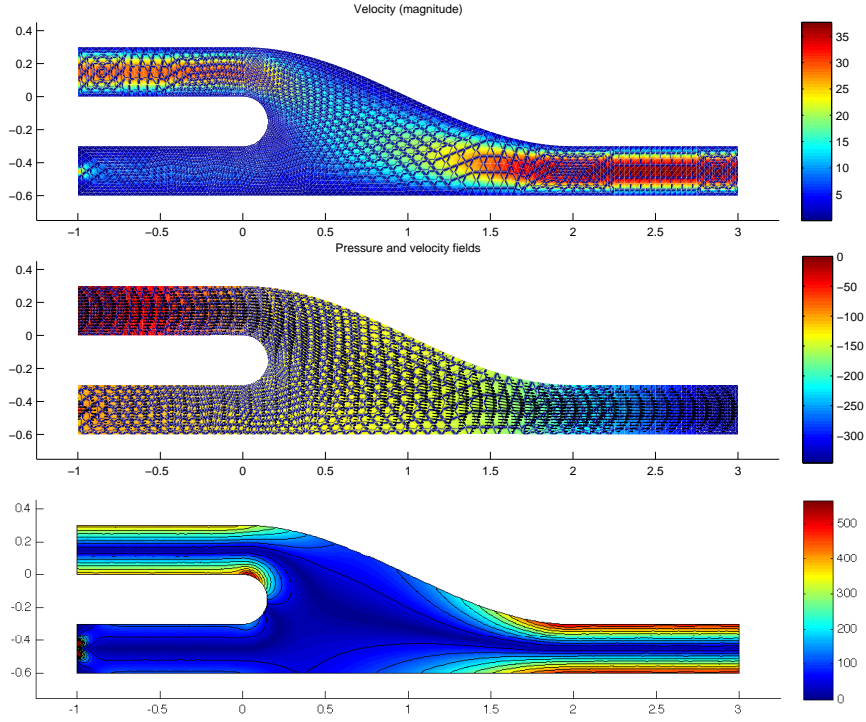
Figure 14: Test B: velocity field, pressure field and vorticity magnitude for the reference configuration.

as clinically significant as the high vorticity values near the toe region and in the down-field region, which is a well-known location where restenosis might reform. The shape optimization procedure however enables to reduce the vorticity in the down-field region of the anastomosis, even if increasing values of vorticity arise at heel and top segments. In the case where the observation region Ω_{obs} is the whole domain Ω instead of the subdomain Ω_{df} – and thus vorticity is minimized all over the anastomosis – different results can be obtained, both in terms of optimal shapes and vorticity reduction. By using the same procedure as before, we obtain (e.g. for test case B) the vorticity patterns in Fig. 16: the minimization of the vorticity all over the anastomosis leads to optimal shapes characterized by bigger sections and narrow bifurcations. Moreover, the parameter μ_5 – which strongly affects the anastomotic angle – seems to play an important role in the behavior of the vorticity field. For both test cases numerical results are summarized in Tabs. 1 and 2.

8.2   Computational features

Reduced basis techniques, combined with a free-form deformation framework for shape optimization, allow a substantial reduction of both geometrical complexity and computational work. An iterative optimization procedure is greatly
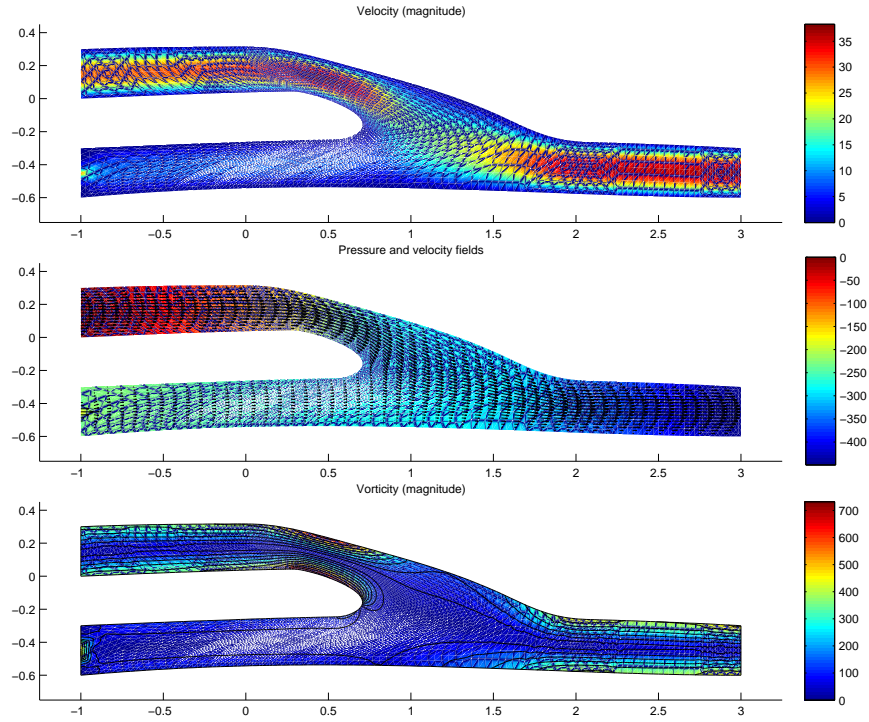
Figure 15: Test B: velocity field, pressure field and vorticity magnitude for the optimal configuration.
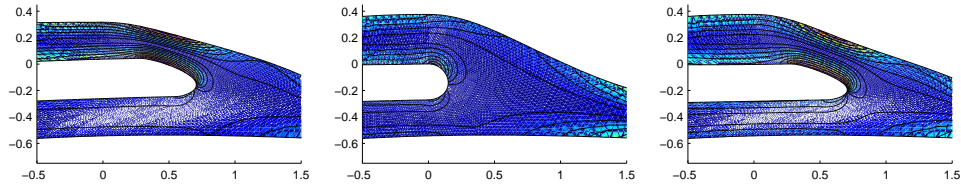

Figure 16: Test B: optimal shapes (and related vorticity patterns) obtained through vorticity minimization on the down-field region Ω_{df} (left) and on the whole domain Ω (middle, right). In the third case the parameter μ_5 has been fixed equal to the optimal value obtained in the first case by vorticity minimization on Ω_{df}.

enhanced by the computational gain since at each step the cost functional to be minimized is evaluated using the RB approximation. Compared to a flow simulation by finite elements, in our 2D aorto-coronaric bypass case, a RB On-line evaluation of flow variables enables a computational speedup of about 100 times. In particular, the average time over 100 Online evaluations is of 2.204 seconds for the test case A and of 2.012 seconds for the test case B, while the corresponding FE computations take an average time of 209 and 216 seconds, respectively. More details are reported in Tab. 3. This is basically due to the

Ω_{obs}	$s_N(\boldsymbol{\mu}^{(0)})$	$s_N(\hat{\boldsymbol{\mu}})$	Δs_N	# iterations	cpu (s)
Ω_{df}	0.680	0.301	56%	36	2968
Ω	1.103	0.580	47%	45	3504

Table 1: Test case A: initial and optimal value of cost functional, total reduction, number of iterations of the optimization procedure and cpu times for a vorticity observation on Ω_{df} and Ω.

Ω_{obs}	$s_N(\boldsymbol{\mu}^{(0)})$	$s_N(\hat{\boldsymbol{\mu}})$	Δs_N	# iterations	cpu (s)
Ω_{df}	1.249	0.458	63%	45	3554
Ω	1.830	0.823	55%	158	10492

Table 2: Test case B: initial and optimal value of cost functional, total reduction, number of iterations of the optimization procedure and cpu times for a vorticity observation on Ω_{df} and Ω.

reduction of about 500 times in the dimension of the linear systems obtained by finite element discretization and reduced basis approximation: in the first case, we get a sparse linear system of dimension $35,997$ while in the second case linear systems – which are now of full type – have dimension 72 and 66, for the test case A and B, respectively. Consequently, computational times for the whole optimization process are reduced too, depending almost linearly by the time for a single Online evaluation.

Moreover, a shape parametrization based on FFD allows a strong reduction in geometrical complexity: indeed, geometrical reduction in term of the number of parameters is of about 100 with respect to traditional shape parametrization based on local boundary variation. However, by acting on a small set of design variables it is possible to describe a wide family of shapes and thus perform optimization in a low dimensional but quite rich space of admissible configurations. On the one hand, by properly choosing the location of the parameters, FFD enables not to constrain *a priori* the shape of a configuration too similar with respect to the initial one, as in the case where affine or non-affine mappings on different subdomains are used [17, 13], and make the upper wall free to deform; on the other hand, it allows a strict control on those parts where a shape is in some sense prescribed (as in the case of the lower wall).

9 Conclusions and further developments

The purpose of the present work has been to develop a new model order reduction strategy for shape optimization by coupling reduced basis methods for flow simulation with free-form deformation techniques for shape parametrization. This framework has been applied to an optimal design problem of an aorto-coronaric

	FE	RB (min)	RB (average)	RB (max)	Speedup
Test Case A	209.06s	1.939s	2.012s	3.078s	94.85
Test Case B	215.76s	1.945s	2.204s	3.314s	107.18

Table 3: Computational times and speedup for reduced basis Online evaluations and finite element computations. RB Online evaluations have been executed considering a sample of 100 randomly chosen parameter vectors $\boldsymbol{\mu} \in \mathcal{D}$.

bypass anastomosis, allowing a deep reduction in both computational efforts (w.r.t. classical strategies based on finite element discretization techniques) and geometrical complexity (w.r.t. more traditional shape parametrization approaches). A reduced basis formulation has been discussed for noncoercive problems, taking advantage of the empirical interpolation method to deal with the nonaffine parametric dependence. A free-form deformation setting has been presented and applied to a complex 2D configuration.

In order to get more precise results and deal with more complex fluid dynamics, the extension of this framework to Navier-Stokes equations and 3D configurations is in order and represents our current research activity. The accuracy of future simulations and optimization stages is dependent, as underlined by Loth and al. [24], on the acquisition of patient-specific data such as geometry properties or flow conditions. Following this path, we intend to consider in the next future a coupled parametrization of both geometrical and flow physical properties, such as rheology or boundary conditions. Moreover, an efficient characterization of a posteriori error estimators for quadratic output is currently under investigation.

Acknowledgements

References

[1] G. Allaire, Conception optimale de structures, Springer, vol. 58 Mathématiques et Applications, 2007.

[2] J. Haslinger, R. Mäkinen, Introduction to shape optimization: theory, approximation, and computation, SIAM, 2003.

[3] T. Lehnhäuser, M. Schäfer, A numerical approach for shape optimization of fluid flow domains, Comput. Methods Appl. Mech. Eng. 194 (2005) 5221–5241.

[4] B. Mohammadi, O. Pironneau, Applied shape optimization for fluids, Oxford University Press, 2001.

[5] E. Amoiralis, I. Nikolos, Freeform deformation versus B-spline representation in inverse airfoil design, J. Comput. Inf. Sci. En. 8 (2).

[6] M. Botsch, I. Kobbelt, Freeform shape representations for efficient geometry processing, International Conference on Shape Modeling and Applications.

[7] T. Sederberg, S. Parry, Free-form deformation of solid geometric models, Comput. Graph. 20(4) (1986) 151–160.

[8] A. Patera, G. Rozza, Reduced Basis Approximation and A Posteriori Error Estimation for Parametrized Partial Differential Equations, Version 1.0, Copyright MIT, to appear in (tentative rubric) MIT Pappalardo Graduate Monographs in Mechanical Engineering., 2009, available at http://augustine.mit.edu.

[9] G. Rozza, D. Huynh, A. Patera, Reduced basis approximation and a posteriori error estimation for affinely parametrized elliptic coercive partial differential equations, Arch. Comput. Methods Eng. 15 (2008) 229–275.

[10] M. Barrault, Y. Maday, N. Nguyen, A. Patera, An 'empirical interpolation' method: application to efficient reduced-basis discretization of partial differential equations, C. R. Math. Acad. Sci. Paris 339 (9) (2004) 667–672.

[11] M. Grepl, Y. Maday, N. Nguyen, A. Patera, Efficient reduced-basis treatment of nonaffine and nonlinear partial differential equations, Esaim Math. Model. Numer. Anal. 41 (3) (2007) 575–605.

[12] N. Nguyen, A posteriori error estimation and basis adaptivity for reduced-basis approximation of nonaffine-parametrized linear elliptic partial differential equations, J. Comput. Phys. 227 (2007) 983–1006.

[13] G. Rozza, Shape design by optimal flow control and reduced basis techniques: applications to bypass configurations in haemodynamics, Ph.D. thesis, N. 3400, École Polytechnique Fédérale de Lausanne (2005).

[14] A. Quarteroni, G. Rozza, Optimal control and shape optimization of aorto-coronaric bypass anastomoses, Math. Models Meth. Appl. Sci. 13 (12) (2003) 1801–1823.

[15] V. Agoshkov, A. Quarteroni, G. Rozza, A mathematical approach in the design of arterial bypass using unsteady Stokes equations, SIAM J. Sci. Comput. 28 (2/3) (2006) 139–165.

[16] V. Agoshkov, A. Quarteroni, G. Rozza, Shape design in aorto-coronaric bypass anastomoses using perturbation theory, SIAM J. Numer. Anal. 44 (1) (2006) 367–384.

[17] G. Rozza, Reduced basis methods for Stokes equations in domains with non-affine parameter dependence, Comput. Vis. Sci. 12(1) (2009) 23–35.

[18] G. Rozza, K. Veroy, On the stability of the reduced basis method for Stokes equations in parametrized domains, Comput. Methods Appl. Mech. Eng. 196 (7) (2007) 1244–1260.

[19] J. Cole, J. Watterson, M. O'Reilly, Is there a haemodynamic advantage associated with cuffed arterial anastomoses?, J. Biomech. 35 (2002) 1337–1446.

[20] J. Cole, J. Watterson, M. O'Reilly, Numerical investigation of the haemodynamics at a patched arterial bypass anastomosis, Med. Eng. Phys. 24 (2002) 393–401.

[21] T. Frauenfelder, E. Boutsianis, T. Schertler, L. Husmann, S. Leschka, D. Poulikakos, B. Marincek, H. Alkadhi, Flow and wall shear stress in end-to-side and side-to-side anastomosis of venous coronary artery bypass grafts, Biomed. Eng. Online 35 (6).

[22] P. Parang, R. Arora, Coronary vein graft disease: Pathogenesis and prevention, Can. J. Cardiol. 25 (2) (2009) e57–e62.

[23] L. Formaggia, A. Quarteroni, A. Veneziani, Cardiovascular Mathematics. Modeling and simulation of the circulatory system, Springer, Series MS&A, Vol. 1, 2009.

[24] F. Loth, P. Fischer, H. Bassiouny, Blood flow in end-to-side anastomoses, Annu. Rev. Fluid. Mech. 40 (2008) 367–393.

[25] M. Lei, J. Archie, C. Kleinstreuer, Computational design of a bypass graft that minimizes wall shear stress gradients in the region of the distal anastomosis, J. Vasc. Surg. 25 (4) (1997) 637–646.

[26] M. Sankaranarayanan, L. Chua, D. Ghista, Y. Tan, Computational model of blood flow in the aorto-coronary bypass graft, Biomed. Eng. Online 4(14).

[27] F. Xiong, C. Chong, A parametric numerical investigation on haemodynamics in distal coronary anastomoses, Med. Eng. Phys. 30 (3) (2008) 311–320.

[28] M. Gunzburger, Perspectives in Flow Control and Optimization, SIAM, 2003.

[29] M. Gunzburger, H. Kim, S. Manservisi, On a shape control problem for the stationary Navier-Stokes equations, Esaim Math. Model. Num. Anal. 34 (6) (2000) 1233–1258.

[30] J. Céa, S. Garreau, P. Guillaume, M. Masmoudi, The shape and topological optimizations connection, Comput. Methods Appl. Mech. Eng. 188 (2000) 713–726.

[31] M. Delfour, J.-P. Zolésio, Shapes and geometries - analysis, differential calculus, and optimization, SIAM, 2001.

[32] J. Sokolowski, J.-P. Zolésio, Introduction to shape optimization: shape sensitivity analysis, Springer-Verlag, 1992.

[33] A. Henrot, M. Pierre, Variation et optimisation de formes. Une analyse géométrique, Springer, Series Mathématiques et Applications, Vol. 48, 2005.

[34] F. Bélahcène, J. Désidéri, Paramétrisation de Bézier adaptative pour l'optimisation de forme en Aérodynamique, INRIA, Rapp. de rech. no. 4943.

[35] A. Clarich, J. Désidéri, Self-adaptive parametrisation for aerodynamic optimum-shape design, INRIA, Rapp. de rech. no. 4428.

[36] M. Andreoli, A. Janka, J. Désidéri, Free-form-deformation parametrization for multilevel 3D shape optimization in aerodynamics, INRIA, Rapp. de rech. no. 5019.

[37] G. Rozza, A. Manzoni, Model order reduction by geometrical parametrization for shape optimization in computational fluid dynamics, in: Proceedings of ECCOMAS CFD 2010, V European Conference on Computational Fluid Dynamics, Lisbon, Portugal, J.C.F. Pereira and A. Sequeira (Eds), 2010.

[38] A. Quarteroni, Numerical Models for Differential Problems, Springer, Series MS&A , Vol. 2, 2009.

[39] M. Berggren, Numerical solution of a flow-control problem: vorticity reduction by dynamic boundary action, SIAM J. Sci. Comput. 19 (3) (1998) 829–860.

[40] N. Nguyen, K. Veroy, A. Patera, Certified real-time solution of parametrized partial differential equations, in: In: S. Yip (Ed.), Handbook of Materials Modeling, Springer, 2005, pp. 1523–1558.

[41] J. Cea, Conception optimale ou identification de formes: calcul rapide de la dérivée directionelle de la fonction cout, Math. Model. Num. Anal. 20 (3) (1986) 371–402.

[42] T. Lassila, G. Rozza, Parametric free-form shape design with PDE models and reduced basis method, Comput. Methods Appl. Mech. Eng. 199 (2010) 1583–1592.

[43] G. Rozza, T. Lassila, A. Manzoni, Reduced basis approximation for shape optimization in thermal flows with a parametrized polynomial geometric map, in: Proceedings of ICOSAHOM Conference, NTU Trondheim, Norway, June 2009, Springer, Series Lecture Notes in Computational Science and Engineering (in press), 2010.

[44] D. Huynh, G. Rozza, S. Sen, A. Patera, A successive constraint linear optimization method for lower bounds of parametric coercivity and inf-sup stability costants, C. R. Acad. Sci. Paris. Sér. I Math. 345 (2007) 473–478.

[45] D. Huynh, A. Manzoni, G. Rozza, Reduced basis approximation and error bounds for Stokes flows in parametrized geometries, In preparation.

[46] L. Dedè, Adaptive and reduced basis methods for optimal control problems in environmental applications, Ph.D. thesis, Politecnico di Milano (2008).

[47] D. Huynh, N. Nguyen, G. Rozza, A. Patera, Rapid reliable solution of the parametrized partial differential equations of continuum mechanics and transport, `http://augustine.mit.edu` (2008-2010).

[48] F. Saleri, P. Gervasio, G. Rozza, A. Manzoni, `MLIfe`, A Matlab LIbrary for Finite Elements, tutorial (in progress), MOX, Politecnico di Milano and CMCS, Ecole Polytechnique Fédérale de Lausanne. ©Politecnico di Milano.

[49] M. Hinze, R. Pinnau, M. Ulbrich, S. Ulbrich, Optimization with PDE Constraints, Springer, Series Mathematical Modelling: Theory and Applications, Vol. 23, 2009.

MOX Technical Reports, last issues

**Dipartimento di Matematica "F. Brioschi",
Politecnico di Milano, Via Bonardi 9 - 20133 Milano (Italy)**